



OPEN ACCESS

EDITED BY

Mourad Bezzeghoud,
Universidade de Évora, Portugal

REVIEWED BY

Lin Zhang,
Hohai University, China
Jiajia Zhangjia,
China University of Petroleum, China

*CORRESPONDENCE

Jidong Yang,
jidong.yang@upc.edu.cn

SPECIALTY SECTION

This article was submitted to Solid Earth Geophysics, a section of the journal
Frontiers in Earth Science

RECEIVED 13 October 2022

ACCEPTED 15 November 2022

PUBLISHED 27 January 2023

CITATION

Hu Z, Yang J, Han L, Huang J, Qin S, Sun J and Yu Y (2023). Modeling seismic wave propagation in the Loess Plateau using a viscoacoustic wave equation with explicitly expressed quality factor. *Front. Earth Sci.* 10:1069166.
doi: 10.3389/feart.2022.1069166

COPYRIGHT

© 2023 Hu, Yang, Han, Huang, Qin, Sun and Yu. This is an open-access article distributed under the terms of the [Creative Commons Attribution License \(CC BY\)](#). The use, distribution or reproduction in other forums is permitted, provided the original author(s) and the copyright owner(s) are credited and that the original publication in this journal is cited, in accordance with accepted academic practice. No use, distribution or reproduction is permitted which does not comply with these terms.

Modeling seismic wave propagation in the Loess Plateau using a viscoacoustic wave equation with explicitly expressed quality factor

Ziduo Hu¹, Jidong Yang^{2*}, Linghe Han¹, Jianping Huang², Shanyuan Qin², Jiaxing Sun² and Youcai Yu²

¹Research Institute of Petroleum Exploration and Development-Northwest PetroChina, Lanzhou, China, ²School of Geosciences, Laboratory for Marine Mineral Resources, National Laboratory for Marine Science and Technology, China University of Petroleum (East China), Qingdao, Shandong, China

The thick Quaternary loess on the Loess Plateau of China produces strong seismic attenuation, resulting in weak reflections from subsurface exploration targets. Accurately simulating seismic wavefield in the Loess Plateau is important for guiding subsequent data processing and interpretation. We present a 2D/3D wavefield simulation method for the Loess Plateau using a viscoacoustic wave equation with explicitly expressed quality factor. To take into account the effect of irregular surface, we utilize a vertically deformed grid to represent the topography, and solve the viscoacoustic wave equation in a regular computational domain that conforms to topographic surface. Grid deformation introduces the partial derivatives such as $\partial v_x / \partial z$ and $\partial v_y / \partial z$ in the wave equation, which is difficult to be accurately computed using traditional staggered-grid finite-difference method. To mitigate this issue, a finite-difference scheme based on a fully staggered-grid is adopted to solve the viscoacoustic wave equation. Numerical experiments for a simple layer model and 2D/3D realistic Loess Plateau models demonstrate the feasibility and adaptability of the proposed method. The 3D modeling results show comparable amplitude and waveform characteristics to the field data acquired from the Chinese Loess Plateau, suggesting a good performance of the proposed modeling method.

KEYWORDS

viscoacoustic modeling, seismic wave attenuation, Loess Plateau, topographic surface, computational seismology

Introduction

Seismic modeling always plays an important role in the study of wave phenomenon, and provides numerical propagators for seismic imaging and inversion (Bording and Lines, 1997; Virieux et al., 2009). According to theoretical background and numerical implementation, seismic modeling approaches can be categorized into two basic groups (Carcione et al., 2002): ray-based and wave-equation methods. Each group has its own pros and cons, and both of them have been widely used in seismic modeling, imaging and inversion.

Seismic ray is a high-frequency asymptotic solution of the wave equation (Červený, 2001), of which the traveltime and amplitude are determined by the eikonal and transport equations, respectively. It decomposes the coupled wavefields into independent single-phase waves, including direct wave, reflection, refraction, transmission, converted wave, multiples, etc (Červený et al., 2007). This makes it easy to study a specific wave phenomenon in complicated subsurface structures. In the past half century, ray-based methods have evolved from classical kinematic ray tracing (Julian and Gubbins, 1977; Um and Thurber, 1987), through paraxial ray tracing (Beydoun and Keho, 1987) and Maslov asymptotic theory (Maslov et al., 1972; Chapman and Drummond, 1982; Kendall and Thomson, 1993), then to Gaussian beam (Červený et al., 1982; Müller, 1984; Nowack and Aki, 1984). Due to high computational efficiency, ray-based Kirchhoff and beam migrations have become routine tools for seismic imaging and migration velocity analysis in the industry (Hill, 1990, 2001; Gray and May 1994; Yang et al., 2018, 2022).

The other group of seismic modeling is to directly solve the wave equation onto a discretized grid using numerical solvers. Typical numerical algorithms include finite-difference, finite-element, pseudo-spectrum, spectrum-element and boundary-element approaches (Carcione et al., 2002). Because of relatively cheap cost, the finite-difference has been extensively used for wavefield simulation (Kristek and Moczo, 2003; Etgen and O'Brien, 2007), reverse-time migration (McMechan, 1989; Wu et al., 1996) and full-waveform inversion (Mulder and Plessix, 2008; Vigh et al., 2009; Virieux and Operto, 2009) in exploration seismology. Using the triangle or tetrahedral mesh to discretize the geological model, the finite-element approach can accurately simulate wave propagation in strong heterogeneous media (Marfurt, 1984; De Basabe and Sen, 2009; Komatitsch et al., 2010). But due to large computational cost, it is usually limited for small-scale problems, e.g., in the fault zone and oil & gas reservoir. The spectrum-element method inherits the flexibility of finite-element and the accuracy of spectral method, and the diagonal mass matrix using a specific discretization and integration rule results in a higher efficiency than finite-element method (Komatitsch and Tromp, 1999; Komatitsch et al., 2000; Komatitsch and Tromp, 2002). These advantages make it have been widely applied to wavefield simulation and adjoint tomography in regional and global seismology (Komatitsch et al., 2002; Tape et al., 2009; Lei et al., 2020).

The Loess Plateau of China has the thickest and largest loess coverage in the world, which was deposited in the Pleistocene under

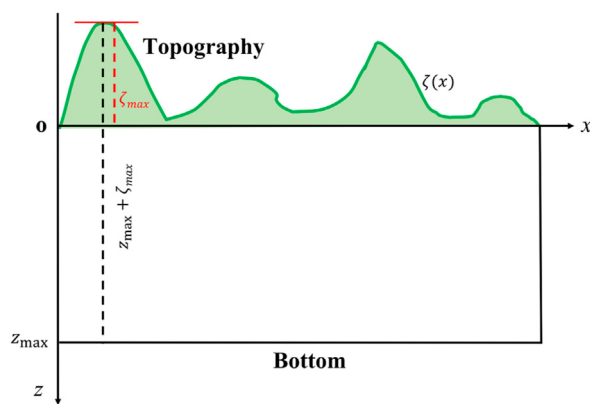
TABLE 1 The weights and decay times of three relaxation mechanisms used in the viscoacoustic modeling.

Weights	Value	Decay times	Value
$D^{(1)}$	1.74278563	$\tau^{(1)}$	0.00159180
$D^{(2)}$	1.41221145	$\tau^{(2)}$	0.01450505
$D^{(3)}$	1.72183357	$\tau^{(3)}$	0.14020500

particular geological, geomorphological and climatic conditions (Sun, 2002). Rich oil and gas resource under the loess promote extensive seismic exploration in this area. Low-velocity loess layer and complicated topography produce strong seismic attenuation and scattering noise, resulting in deep reflections with a very low signal-to-noise ratio (SNR). The low-quality observed data present a large challenge for subsequent processing and interpretation (Wang et al., 2004; Wang et al., 2014). Accurately simulating the wavefields of the Loess Plateau helps to understand noise generation mechanism and attenuation effect of thick loess layer, which can guide subsequent data processing and imaging. In the wavefield modeling for the Loess Plateau, it is necessary to take into account the irregular topography and strong attenuation due to complex near-surface geology.

There are many rheological models to characterize seismic attenuation during wave propagation. For instance, a complex-valued velocity can be directly introduced into the frequency-domain wave equation to describe phase dispersion and amplitude dissipation (Liao and McMechan, 1996; Stekl and Pratt, 1998; Aki and Richards, 2002). On the other hand, in the time domain, the nearly constant attenuation effect within a frequency band can be implemented by a combination of springs and dashpots in series and/or parallel (Carcione, 2007). Typical viscous models include classical and generalized Maxwell body (Emmerich and Korn, 1987), Kelvin-Voigt body (Carcione et al., 2004), and standard linear solid body (Liu et al., 1976; Carcione, 1993; Guo et al., 2019). Using a fractional time derivative, Kjartansson (1979) presented an alternative constant quality factor (Q) model to describe the stress and strain relation. Zhu and Harris (2014) utilized a fractional Laplacian operator to approximate the fractional time derivative and obtained a simplified constant- Q wave equation. Later, many hybrid-domain solvers, including local homogeneous approximation (Chen et al., 2016; Wang et al., 2017; Xing and Zhu, 2019; Wang et al., 2022), low-rank approximation (Sun et al., 2015), Hermite distributed approximation (Yao et al., 2017), are proposed to produce more accurate numerically solution. Recently, Yang and Zhu (2018) presented a complex-valued wave equation to simulate viscoacoustic wave propagation, which has an explicitly expressed Q and can be easily used in full-waveform inversion (Yang et al., 2020).

The Loess Plateau of China has diverse geomorphic features, such as hill, tableland, ditch, ridges and mounds, which results into a complex irregular topography. In seismic modeling using the finite-difference, many strategies have been developed to handle topography and free surface. Levander (1988) implemented a flat free-surface

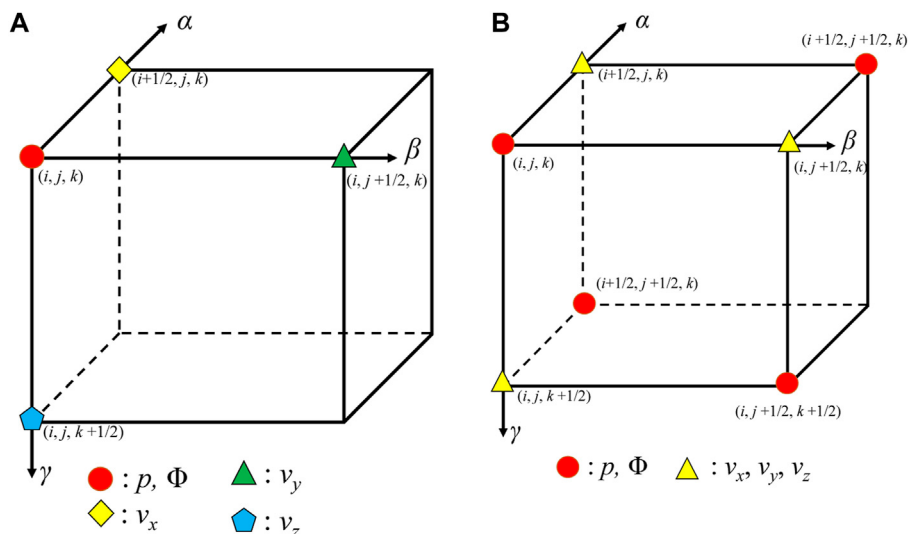
**FIGURE 1**

An example of 2D topography to illustrate the basic parameters in the mapping from the physical space to computational domain.

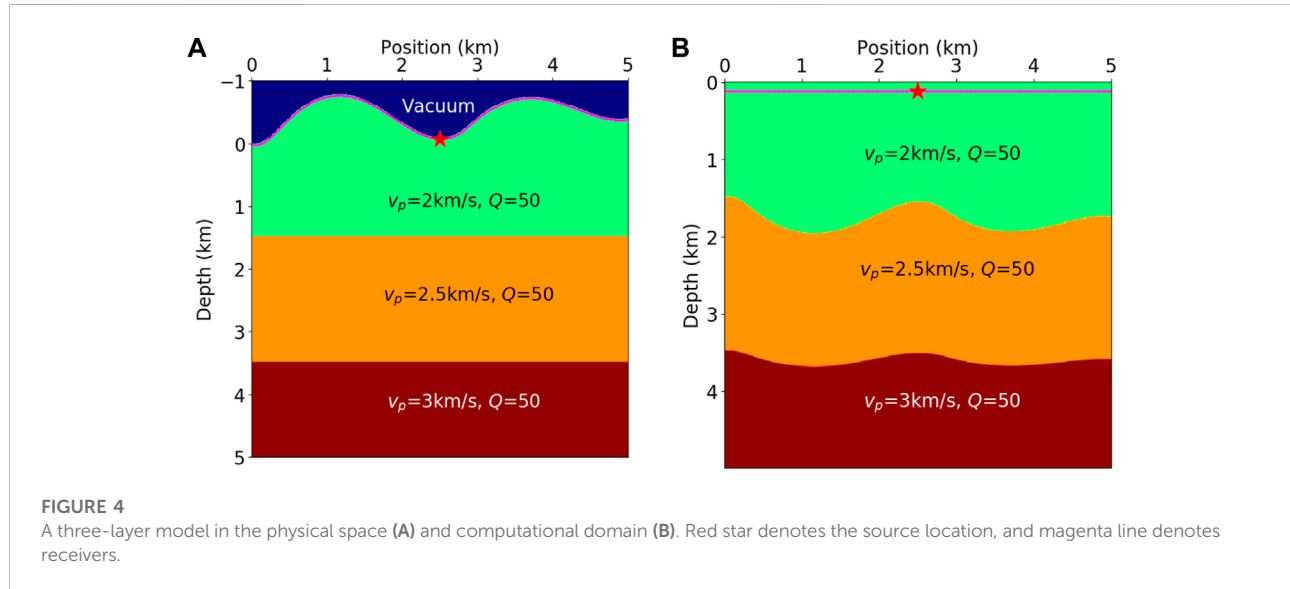
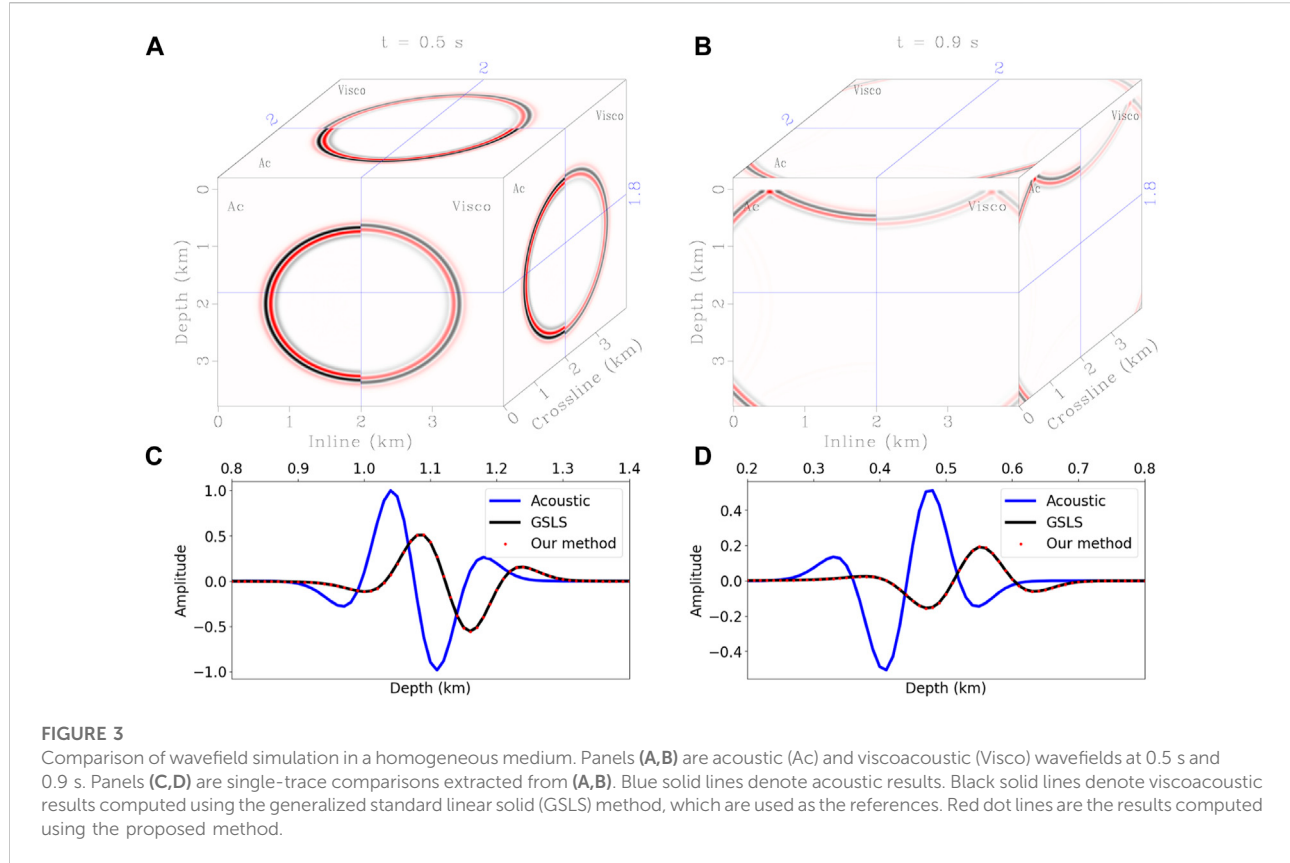
boundary condition using the image method. Later, this approach was extended to highly irregular topography by Robertsson (1996). Mittet (2002) treated elastic Hooke's tensor on the free surface as that in a transversely isotropic medium and presented a simple implementation of free-surface. Nakamura et al. (2012) proposed an efficient Heterogeneity, Oceanic layer and Topography (HOT) finite-difference method to compute wavefields at the solid-air, fluid-air and fluid-solid boundaries. Instead of directly representing the topography at a regularly and densely sampled Cartesian grid, an alternative way is to transform the physical curved domain to a regular computational grid (Hestholm and Ruud, 1994; Hestholm and Ruud, 1998). This curvilinear transformation can avoid the strong scatterings from the staircase topography and is relatively easily to implement the

free-surface condition (Hestholm, 1999; Hestholm and Ruud, 2002; Zhang et al., 2012). At current stage, this approach has been extended to conform both topographic surface and interior layers in viscous and anisotropic media (Sun et al., 2016; Shragge and Tapley, 2017; Konuk and Shragge, 2020; Sun et al., 2021).

In this work, we present a viscoacoustic modeling method to study seismic wave phenomena in the Loess Plateau. A viscoacoustic wave equation is first derived based on a non-linear optimization for the frequency-independent Q effect within a frequency band (Fichtner and van Driel, 2014). To conform to the topographic surface, a vertically deformed grid is adopted to transform the irregular domain to a regular computational coordinate (Jastram and Tessmer, 1994; de la Puente et al., 2014). This strategy does not introduce as many additional partial

**FIGURE 2**

Comparison of the node distribution in the standard (A) and fully (B) staggered-grid finite-difference methods. p denotes the pressure wavefield, Φ denotes the memory variable, and v_{x_i} ($x_i=x, y, z$) denotes particle velocity.



derivatives as the curvilinear grid method that deforms along three axes, and thus it does not increase too much computational cost compared with that computed on traditional Cartesian grid. In addition, to accurately compute the spatial derivatives such as $\partial v_x / \partial z$ and $\partial v_y / \partial z$, we apply a fully staggered-grid finite-difference scheme (Lisitsa and Vishnevskiy, 2010; de la Puente et al., 2014) to

numerically solve the viscoacoustic wave equation on a vertical deformed grid. Numerical experiments for a simple layer model and 2D/3D Loess Plateau models as well as a comparison between synthetic and field data demonstrate the proposed method can accurately simulate wave propagation in the Loess Plateau with thick loess layers.

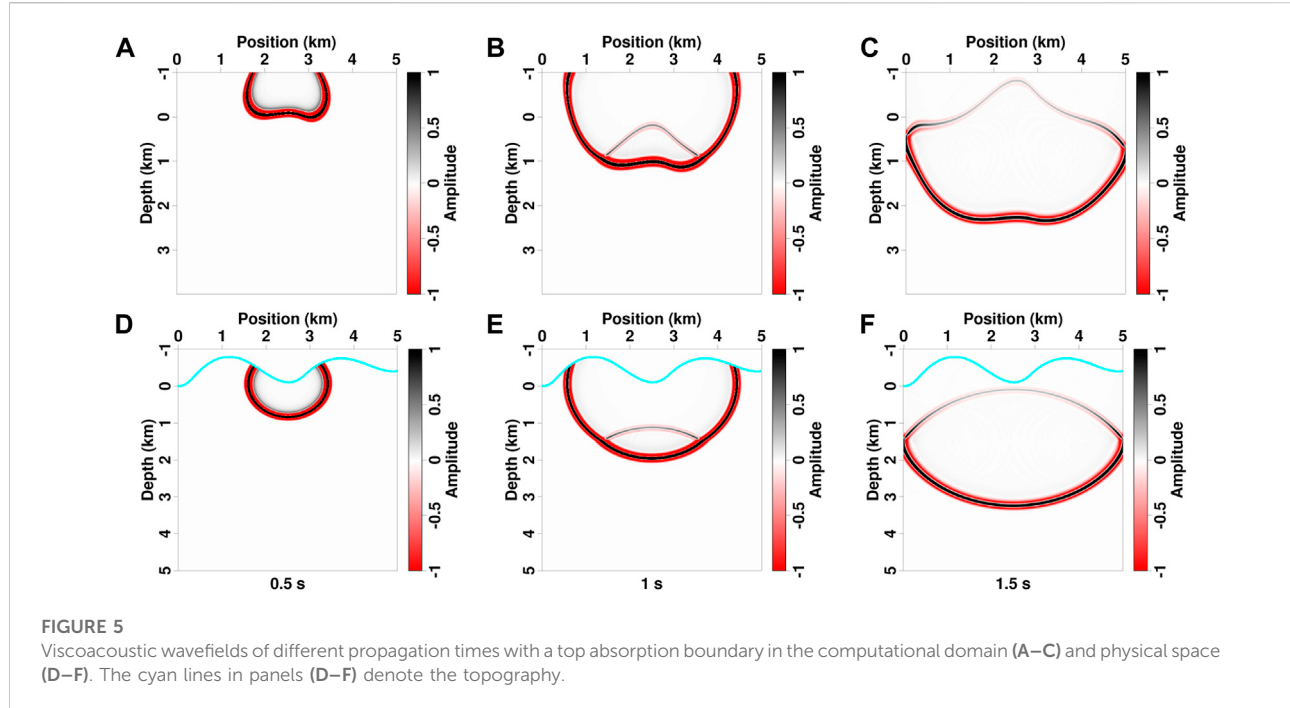


FIGURE 5

Viscoacoustic wavefields of different propagation times with a top absorption boundary in the computational domain (A–C) and physical space (D–F). The cyan lines in panels (D–F) denote the topography.

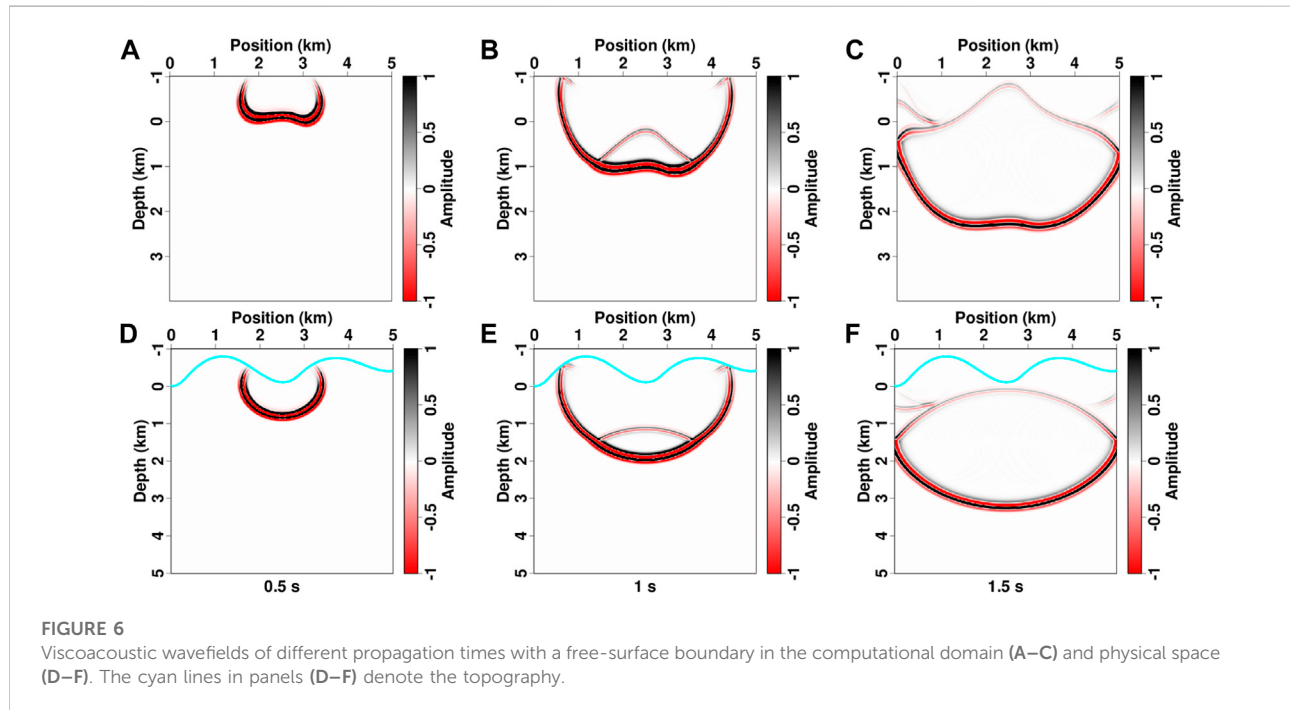


FIGURE 6

Viscoacoustic wavefields of different propagation times with a free-surface boundary in the computational domain (A–C) and physical space (D–F). The cyan lines in panels (D–F) denote the topography.

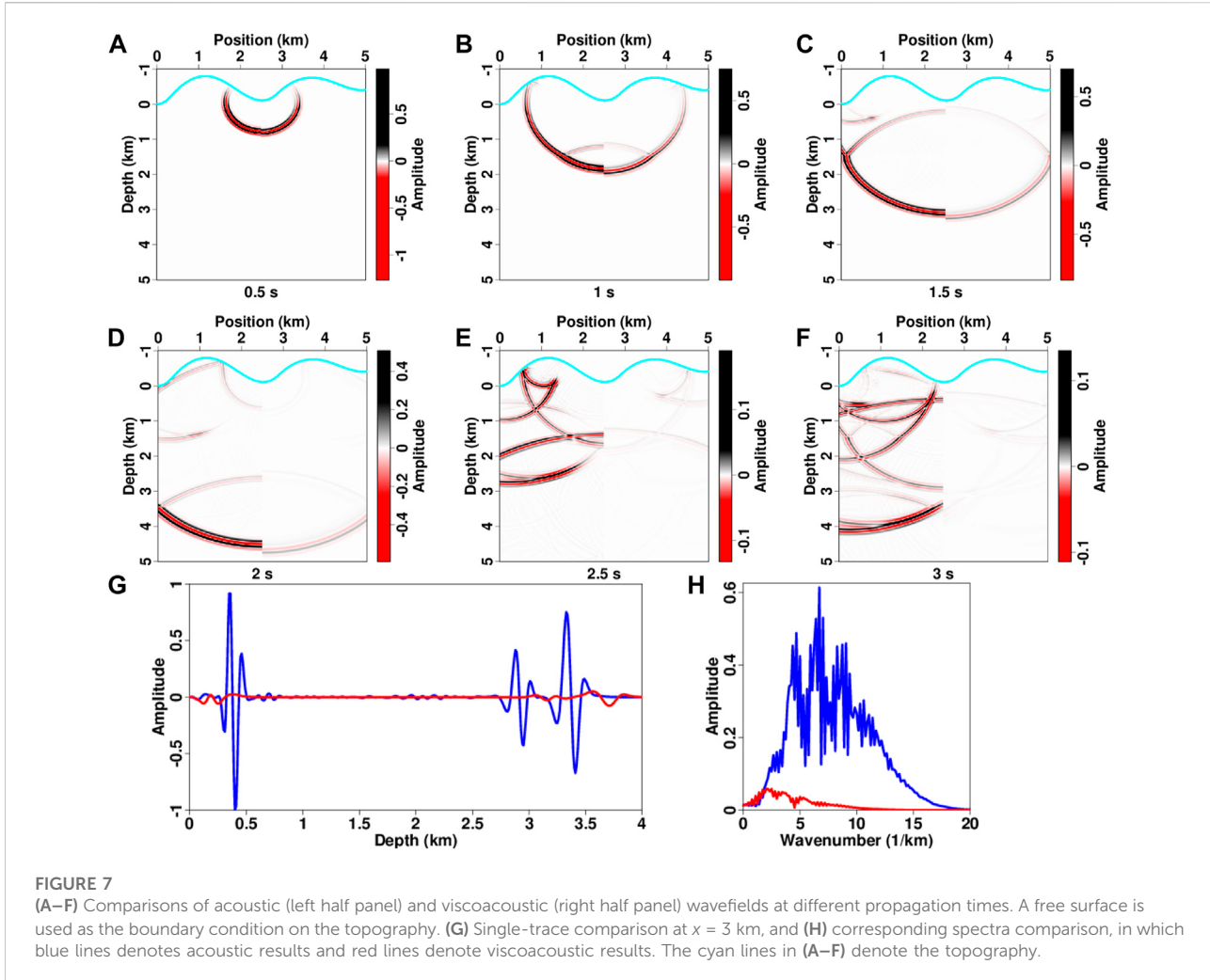
Theory

Viscoacoustic wave equation with explicitly expressed Q

In viscoacoustic medium, the pressure $p(\mathbf{x}, t)$ and particle velocity $\mathbf{v}(\mathbf{x}, t)$ satisfy a constitutive relation as

$$\frac{\partial p(\mathbf{x}, t)}{\partial t} = \int_{-\infty}^{\infty} \frac{\partial \kappa(\mathbf{x}, t - t')}{\partial t'} \nabla \cdot \mathbf{v}(\mathbf{x}, t') dt', \quad (1)$$

where $\mathbf{v} = (v_x, v_y, v_z)$, and subscripts x, y and z denote particle velocity components along different axes. $\kappa(\mathbf{x}, t)$ is a time-dependent bulk modulus and can be constructed by superposing N groups of relaxation mechanisms (Fichtner and van Driel, 2014):



$$\kappa(\mathbf{x}, t) = \kappa_0(\mathbf{x}) \left[1 + \frac{1}{Q(\mathbf{x})} \sum_{l=1}^N D^{(l)} \exp\left(-\frac{t}{\tau^{(l)}}\right) \right] H(t), \quad (2)$$

where $\kappa_0(\mathbf{x}) = \rho(\mathbf{x})v_p^2(\mathbf{x})$ is the relaxed bulk modulus, $\rho(\mathbf{x})$ and $v_p(\mathbf{x})$ denote the density and P-wave velocity, $Q(\mathbf{x})$ is the quality factor, and $H(t)$ is the step function. $D^{(l)}$ and $\tau^{(l)}$ ($1 \leq l \leq N$) are the weights and decay times of different relaxation mechanisms, which can be computed by solving a non-linear optimization problem using a simulated annealing process to fit the frequency-independent Q in a limited band. In this study, we set the reference frequency to 1 Hz and the frequency band to [1, 150] Hz with three relaxation mechanisms. The resulting coefficients are shown in Table 1.

Taking the time derivative of $\kappa(\mathbf{x}, t)$, we have

$$\frac{\partial \kappa(\mathbf{x}, t)}{\partial t} = \kappa_0(\mathbf{x}) \left[\frac{1}{Q(\mathbf{x})} \sum_{l=1}^N \left(-\frac{D^{(l)}}{\tau^{(l)}} \exp\left(-\frac{t}{\tau^{(l)}}\right) \right) H(t) + \left(1 + \frac{s}{Q(\mathbf{x})} \right) \delta(t) \right], \quad (3)$$

where $\delta(t)$ is the Kronecker delta function, and s is the summation of weights, i.e., $s = \sum_{l=1}^N D^{(l)}$. Inserting Eq. 3 into the constitutive relation yields

$$\frac{\partial p(\mathbf{x}, t)}{\partial t} = \kappa_0(\mathbf{x}) \left[\left(1 + \frac{s}{Q(\mathbf{x})} \right) \nabla \cdot \mathbf{v}(\mathbf{x}, t) - \frac{1}{Q(\mathbf{x})} \sum_{l=1}^N \Phi^{(l)}(\mathbf{x}, t) \right], \quad (4)$$

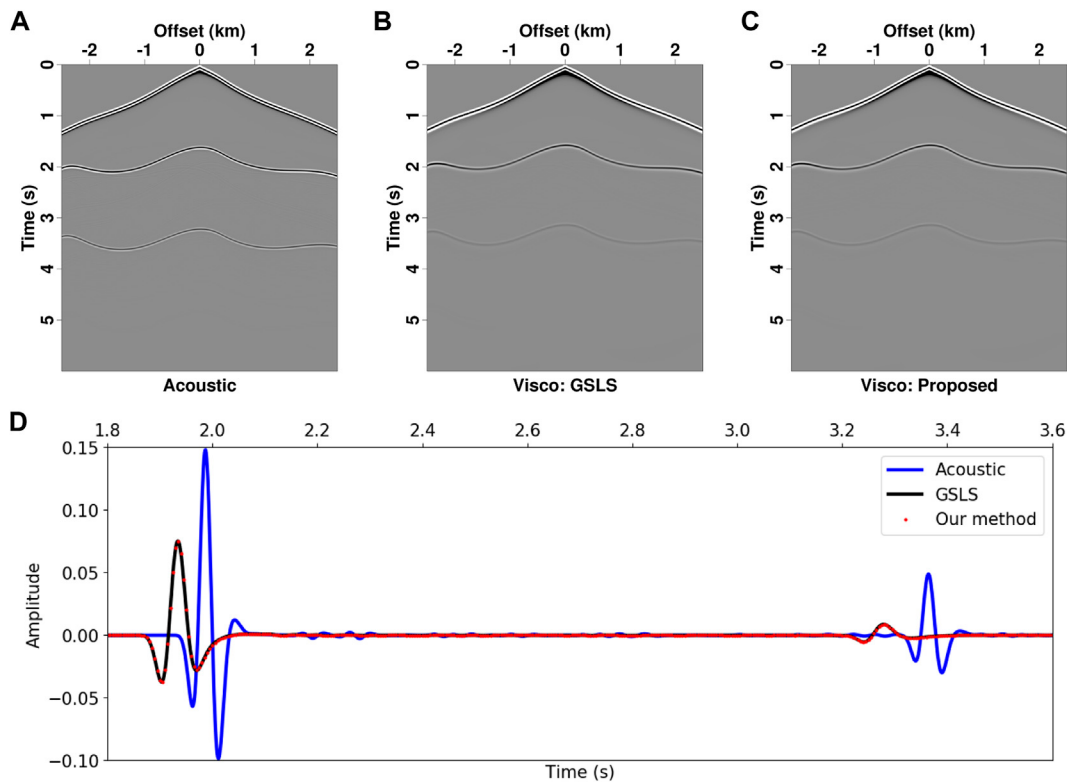
where the memory variables $\Phi^{(l)}(\mathbf{x}, t)$ are defined as

$$\Phi^{(l)}(\mathbf{x}, t) = \frac{D^{(l)}}{\tau^{(l)}} \int_{-\infty}^{\infty} \exp\left(-\frac{t-t'}{\tau^{(l)}}\right) H(t-t') \nabla \cdot \mathbf{v}(\mathbf{x}, t') dt', \quad (5)$$

and satisfy

$$\frac{\partial \Phi^{(l)}(\mathbf{x}, t)}{\partial t} = -\frac{1}{\tau^{(l)}} \Phi^{(l)}(\mathbf{x}, t) + \frac{D^{(l)}}{\tau^{(l)}} \nabla \cdot \mathbf{v}(\mathbf{x}, t). \quad (6)$$

Considering the second Newton law and assembling Eqs 4, 6, we obtain a viscoacoustic wave equation with the explicitly expressed Q as

**FIGURE 8**

Common-shot gathers simulated with a top absorption boundary for the three-layer model. (A) Acoustic modeling, (B) viscoacoustic modeling using the GSLS method, (C) viscoacoustic modeling using the proposed method, and (D) single-trace comparison at the offset of -2.3 km . The amplitudes of panel (D) are normalized by the maximum value of direct waves.

$$\left\{ \begin{array}{l} \rho(\mathbf{x}) \frac{\partial \mathbf{v}(\mathbf{x}, t)}{\partial t} = \nabla p(\mathbf{x}, t), \\ \frac{\partial p(\mathbf{x}, t)}{\partial t} = \rho(\mathbf{x}) v_p^2(\mathbf{x}) \left[\left(1 + \frac{s}{Q(\mathbf{x})} \right) \nabla \cdot \mathbf{v}(\mathbf{x}, t) - \frac{1}{Q(\mathbf{x})} \sum_{l=1}^N \Phi^{(l)}(\mathbf{x}, t) \right] \\ \quad + f(t) \delta(\mathbf{x} - \mathbf{x}_s), \\ \frac{\partial \Phi^{(l)}(\mathbf{x}, t)}{\partial t} = -\frac{1}{\tau^{(l)}} \Phi^{(l)}(\mathbf{x}, t) + \frac{D^{(l)}}{\tau^{(l)}} \nabla \cdot \mathbf{v}(\mathbf{x}, t), \end{array} \right. \quad (7)$$

where \mathbf{x}_s denotes the source location, and $f(t)$ is the source time function.

Compared with existing viscoacoustic wave equations, such as the standard linear solid model (Carcione, 1990; Guo and Mcmechan, 2017) and fractional-Laplacian method (Zhu and Harris, 2014; Xing and Zhu, 2019), Eq. 7 has the following advantages in seismic modeling. 1) The quality factor Q is explicitly incorporated in the wave equation, which does not need to be converted to stress and strain relaxation times as in the standard linear solid method. 2) Eq. 7 can be efficiently solved using any time-domain finite-difference schemes, which does not involve the Fourier transform or more complicated mixed-domain

solvers as in the fractional Laplacian based methods. 3) As shown in Fichtner and van Driel (2014), the frequency-dependent Q effect can also be simulated by recomputing the weights $D^{(l)}$ and relaxation times $\tau^{(l)}$.

Representation of the topographic surface on vertically deformed grids

To conform to the topographic surface of the Loess Plateau, here we use a vertically deformed grid to map the irregular physical space $\mathbf{x} = (x, y, z)$ to a regular computational domain $\alpha = (\alpha, \beta, \gamma)$, which is given by

$$\left\{ \begin{array}{l} \alpha = x, \\ \beta = y, \\ \gamma = \gamma_{max} \frac{z + \zeta(x, y)}{z_{max} + \zeta(x, y)}, \end{array} \right. \quad (8)$$

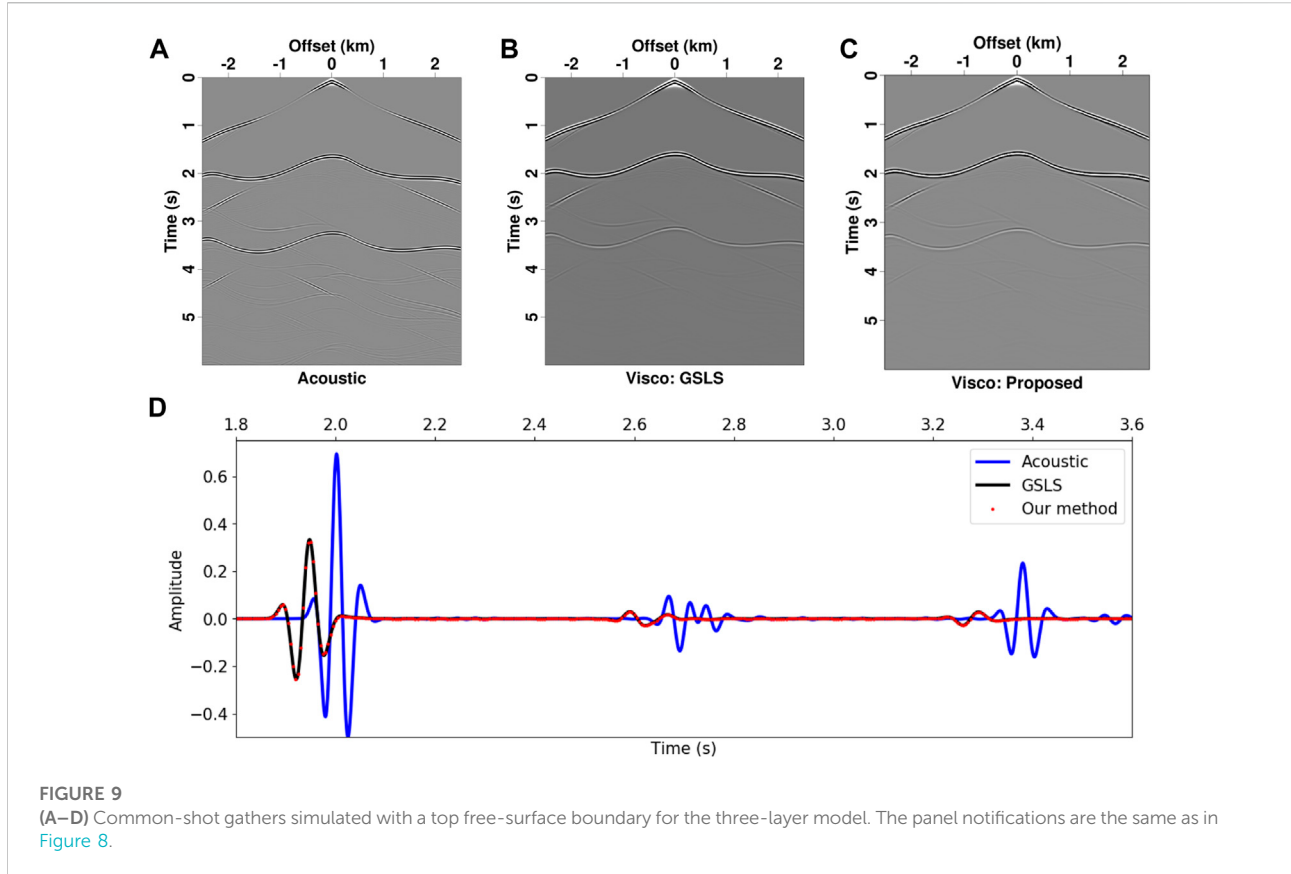


FIGURE 9

(A–D) Common-shot gathers simulated with a top free-surface boundary for the three-layer model. The panel notifications are the same as in Figure 8.

where $\zeta(x, y)$ is the elevation of topography (Figure 1), z_{max} is the maximum depth of the region of interest, $\gamma_{max} = z_{max} + \zeta_{max}$, and ζ_{max} is the maximum of elevation.

With the coordinate transform relation in Eq. 8, the partial derivatives can be computed as

$$\begin{cases} \frac{\partial}{\partial x} = \frac{\partial}{\partial \alpha} + \left[\frac{\gamma_{max} - \gamma}{z_{max} + \zeta(x, y)} \frac{\partial \zeta(x, y)}{\partial x} \right] \frac{\partial}{\partial \gamma}, \\ \frac{\partial}{\partial y} = \frac{\partial}{\partial \beta} + \left[\frac{\gamma_{max} - \gamma}{z_{max} + \zeta(x, y)} \frac{\partial \zeta(x, y)}{\partial y} \right] \frac{\partial}{\partial \gamma}, \\ \frac{\partial}{\partial z} = \left[\frac{\gamma_{max}}{z_{max} + \zeta(x, y)} \right] \frac{\partial}{\partial \gamma}. \end{cases} \quad (9)$$

By setting

$$\begin{cases} c_x = \frac{\gamma_{max} - \gamma}{z_{max} + \zeta(x, y)} \frac{\partial \zeta(x, y)}{\partial x}, \\ c_y = \frac{\gamma_{max} - \gamma}{z_{max} + \zeta(x, y)} \frac{\partial \zeta(x, y)}{\partial y}, \\ c_z = \frac{\gamma_{max}}{z_{max} + \zeta(x, y)}, \end{cases} \quad (10)$$

The viscoacoustic wave equation in Eq. 7 can be rewritten in the new coordinate as

$$\begin{cases} \rho(\alpha) \frac{\partial \mathbf{v}(\alpha, t)}{\partial t} = \bar{\nabla} p(\alpha, t), \\ \frac{\partial p(\alpha, t)}{\partial t} = \rho(\alpha) v_p^2(\alpha) \left[\left(1 + \frac{s}{Q(\alpha)} \right) \bar{\nabla} \cdot \mathbf{v}(\alpha, t) - \frac{1}{Q(\alpha)} \sum_{l=1}^N \Phi^{(l)}(\alpha, t) \right] \\ \quad + f(t) \delta(\alpha - \alpha_s), \\ \frac{\partial \Phi^{(l)}(\alpha, t)}{\partial t} = -\frac{1}{\tau^{(l)}} \Phi^{(l)}(\alpha, t) + \frac{D^{(l)}}{\tau^{(l)}} \bar{\nabla} \cdot \mathbf{v}(\alpha, t), \end{cases} \quad (11)$$

With a generalized partial derivative operator

$$\bar{\nabla} = \begin{bmatrix} \frac{\partial}{\partial \alpha} + c_x \frac{\partial}{\partial \gamma} \\ \frac{\partial}{\partial \beta} + c_y \frac{\partial}{\partial \gamma} \\ c_z \frac{\partial}{\partial \gamma} \end{bmatrix}. \quad (12)$$

The proposed viscoacoustic wavefield simulation in a vertical stretched grid can be summarized into the following steps. First, with the elevation of topography $\zeta(x, y)$, we compute its derivative with respect to x and y and the topography related coordinate stretching parameters c_x and c_y . Then, the irregular physical space is mapped to a regular

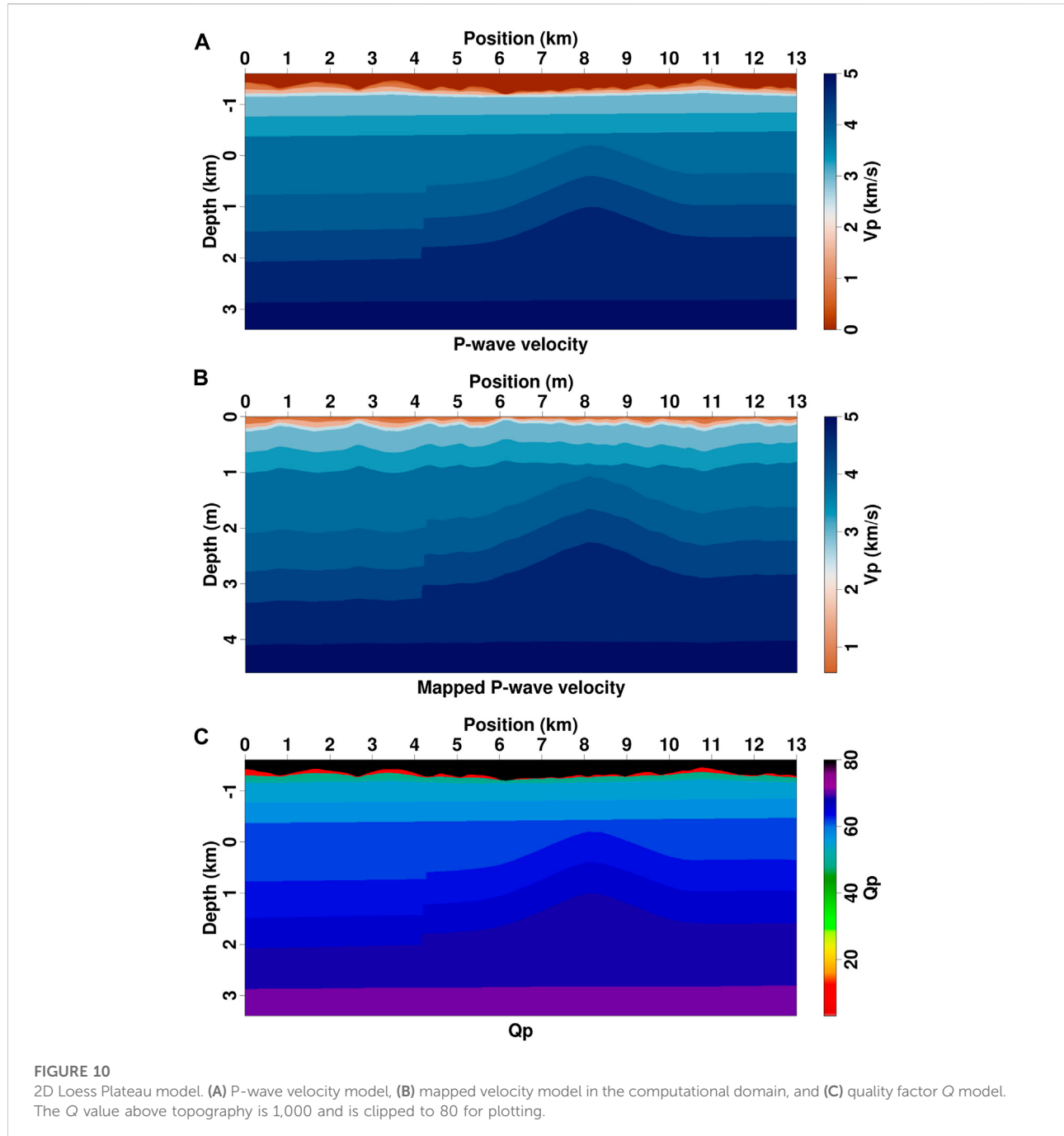


TABLE 2 P-wave velocity and Q values of loess layers.

Layers	P-wave velocity (m/s)	Q Value
Weathering layer	550	5
Low-velocity layer	800	12
Transition layer	1500	48
Tertiary soil layer	2500	70

computational domain by vertical stretching according to Eq. 8, in which velocity, density and Q parameters onto the computational grids are calculated using a linear interpolation method. Next, the viscoacoustic wave equation 11 is solved in a regularly-sampled computational domain using any available numerical solvers. Finally, the wavefields in the real physical space are reconstructed by mapping the extrapolated wavefields back with the same interpolation algorithm used in the second step.

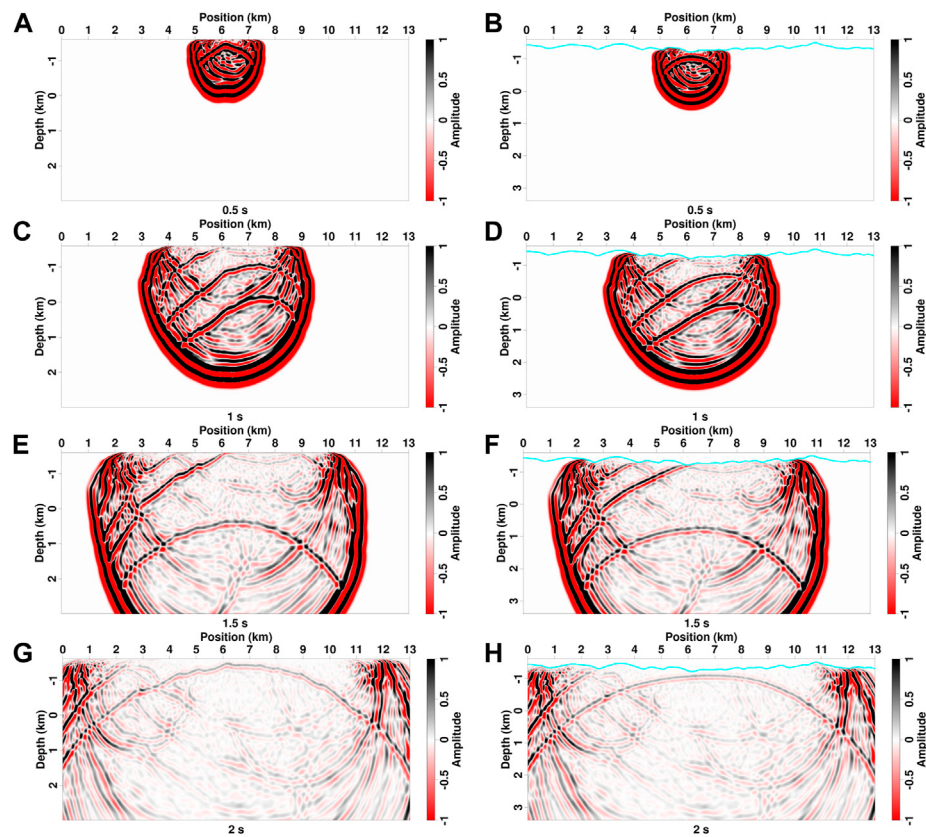


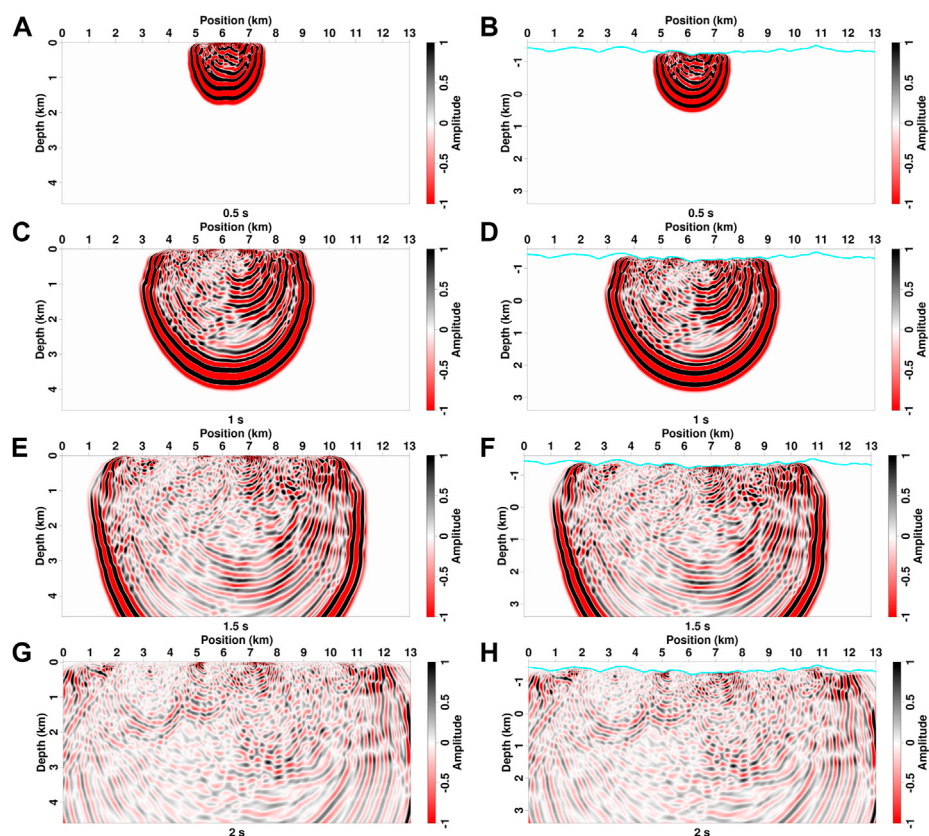
FIGURE 11
(A–H) Viscoacoustic wavefields of 2D Loess Plateau model at different propagation times simulated with a top absorption boundary in the computational domain (left column) and physical domain (right column). The cyan lines in panels (B,D,F, and H) denote the topography.

Numerical implementation using a fully staggered-grid finite difference scheme

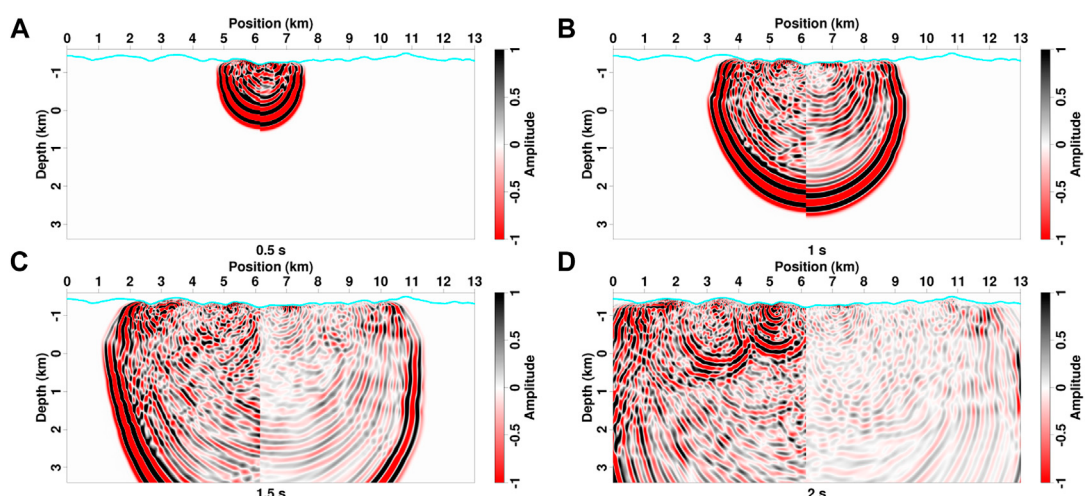
Considering the trade-off of computational accuracy and efficiency, we choose the time-domain staggered-grid finite-difference scheme to solve the viscoacoustic wave Eq. 11. Because of vertical stretching, it is difficult for the standard staggered-grid finite-difference method (Virieux, 1986) to accurately compute the partial derivatives such as $\partial v_x/\partial y$ and $\partial v_y/\partial y$. Here we discretize and solve the wave equation using a fully staggered-grid approach (Lebedev, 1964; Lisitsa and Vishnevskiy, 2010; de la Puente et al., 2014). The nodes distribution is presented in Figure 2. Unlike the standard staggered-grid approach, the fully staggered-grid finite-difference scheme has three particle velocity components at the half grids (yellow triangles in Figure 2B), and three additional pressure wavefields (red circles in Figure 2B). For the time derivative, we still adopt a second-order finite-difference method, which results in the following updating scheme:

$$\left\{ \begin{array}{l} p^{n+1} = p^n + \Delta t \rho v_p^2 \left[\left(1 + \frac{s}{Q} \right) \left((D_\alpha + c_x D_\gamma) v_x^{n+1/2} \right. \right. \\ \left. \left. + (D_\beta + c_y D_\gamma) v_y^{n+1/2} + c_z D_\gamma v_z^{n+1/2} \right) \right] - \frac{1}{2Q} \sum_{l=1}^N (\Phi^{(l),n} + \Phi^{(l),n+1}), \\ \Phi^{(l),n+1} = \frac{1 - \Delta t / (2\tau^{(l)})}{1 + \Delta t / (2\tau^{(l)})} \Phi^{(l),n} + \frac{\Delta t}{1 + \Delta t / (2\tau^{(l)})} \frac{D^{(l)}}{\tau^{(l)}} [(D_\alpha + c_x D_\gamma) v_x^{n+1/2} \\ + (D_\beta + c_y D_\gamma) v_y^{n+1/2} + c_z D_\gamma v_z^{n+1/2}], \\ v_x^{n+3/2} = v_x^{n+1/2} + \frac{\Delta t}{\rho} [D_\alpha p^{n+1} + c_x D_\gamma p^{n+1}], \\ v_y^{n+3/2} = v_y^{n+1/2} + \frac{\Delta t}{\rho} [D_\beta p^{n+1} + c_y D_\gamma p^{n+1}], \\ v_z^{n+3/2} = v_z^{n+1/2} + \frac{\Delta t}{\rho} [c_z D_\gamma p^{n+1}], \end{array} \right. \quad (13)$$

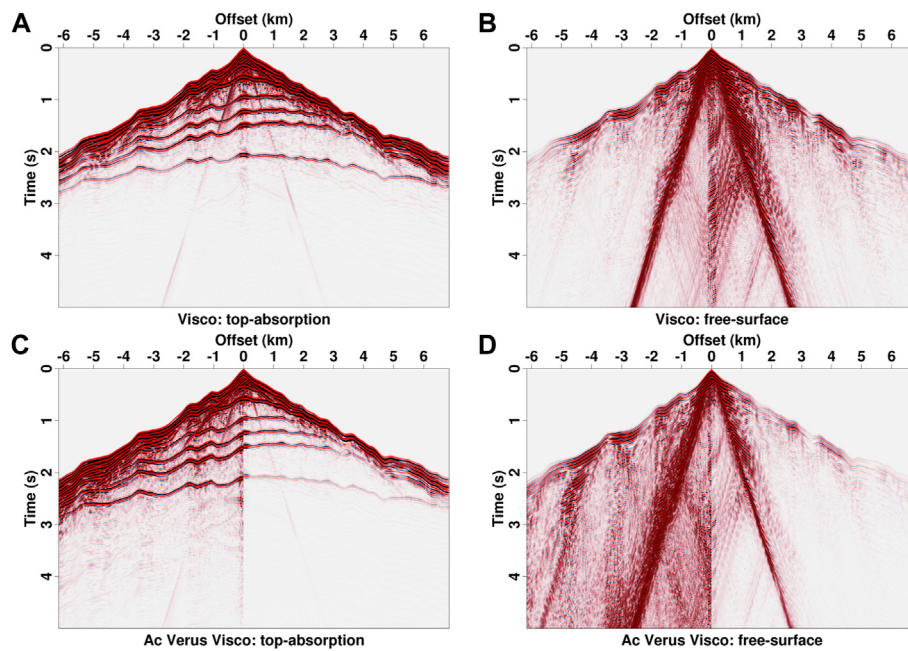
where D_i ($i = \alpha, \beta, \gamma$) denotes the finite-difference operator for first-order spatial derivative. All components of pressure, particle velocity and memory variable wavefields are iteratively computed based on Eq. 13, and each partial derivative can be accurately calculated. Taking p^{n+1} at (i, j, k) as an example, we compute $D_\alpha v_x^{n+1/2}$ and $D_\gamma v_x^{n+1/2}$ using x -component particle velocities at $(i \pm m/2, j, k)$ and

**FIGURE 12**

(A–H) Viscoacoustic wavefields of different propagation times for the 2D Loess Plateau model simulated with a top free-surface boundary in the computational domain (left column) and physical domain (right column). The cyan lines in panels (B,D,F, and H) denote the topography.

**FIGURE 13**

(A–D) Comparison of acoustic (left half panel) and viscoacoustic (right half panel) wavefields for the 2D Loess Plateau model at different propagation times. The cyan lines denote the topography.

**FIGURE 14**

Common-shot gathers of 2D Loess Plateau model (**A,B**) Viscoacoustic modeling with top absorption and free surface boundaries, (**C,D**) comparison of acoustic (left half panel) and viscoacoustic (right half panel) records computed with top absorption and free surface boundaries.

$(i, j, k \pm m/2)$, compute $D_\beta v_y^{n+1/2}$ and $D_\gamma v_y^{n+1/2}$ using y -component particle velocities at $(i, j \pm m/2, k)$ and $(i, j, k \pm m/2)$, and compute $D_\gamma v_z^{n+1/2}$ using z -component particle velocity at $(i, j, k \pm m/2)$, respectively. $m = (1, 2 \dots M)$, where M denotes the half length of finite-difference operator. The other variables at different nodes can be calculated using the same finite-difference scheme. In numerical examples, we set the $M = 4$ and achieve an eighth-order accuracy in space, and the staggered-grid finite-difference coefficients are calculated using the Taylor expansion. To ensure the stability of the finite-difference solver, the temporal increment needs to satisfy the Courant-Friedrichs-Lowy (CFL) condition. In the vertically stretched grid, the relation between time and space increments is (the detailed derivation is given in [Appendix A](#))

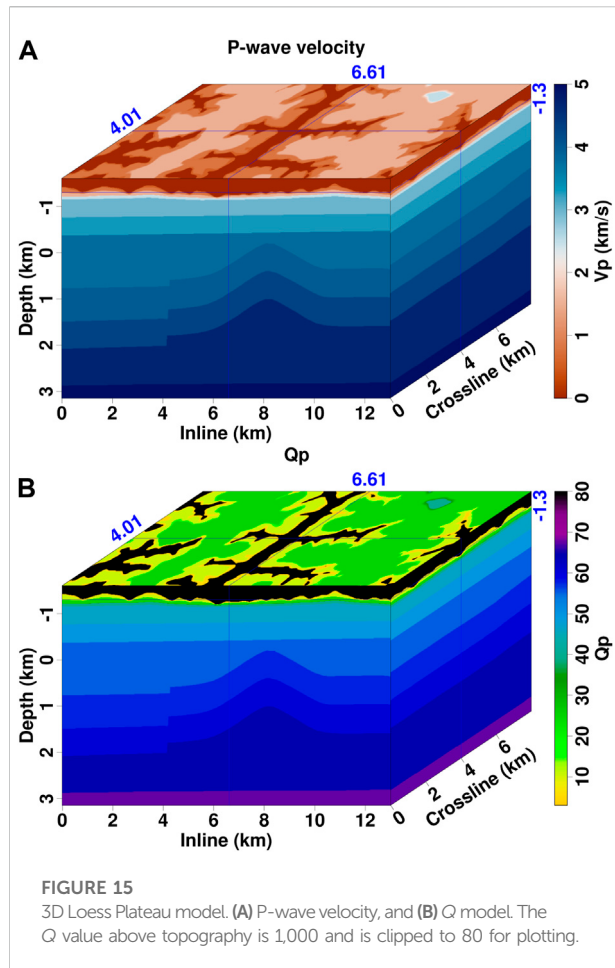
$$\Delta t \leq \frac{\Delta h}{cv_{max} \sqrt{\left(1 + \frac{s}{Q_{min}}\right) \left[(1 + c_{x,max})^2 + (1 + c_{y,max})^2 + (c_{z,max})^2 \right]}}, \quad (14)$$

where c is the summation of finite-difference coefficients, v_{max} denotes the maximum velocity, Q_{min} denotes the minimum quality factor value, and $c_{x_i,max}$ ($x_i = x, y, z$) denotes the maximum value of topography associated coefficients in [Eq. 10](#). For acoustic medium and a flat surface, Q tends to infinity, $c_x = c_y = 0$ and $c_z = 1$. [Eq. 14](#) is simplified to a traditional CFL condition:

$$\Delta t \leq \frac{\Delta h}{\sqrt{3}cv_{max}}. \quad (15)$$

The free-surface boundary condition in the viscoacoustic modeling is implemented using a simple image method ([Zhang et al., 2012](#)). In addition, because two types of grids at different locations are coupled in the fully staggered-grid finite-difference scheme, spurious waves may occur if loading source incorrectly ([Koene et al., 2021](#)). To avoid these spurious waves, we adopt the strategy proposed by [Lisitsa and Vishnevskiy \(2010\)](#) and [de la Puente et al. \(2014\)](#), which is implemented for loading a point source by adding the source function at a node of (i, j, k) and at additional sub-nodes of $(i \pm 1/2, j \pm 1/2, k)$ ($i \pm 1/2, j, k \pm 1/2$), $(i, j \pm 1/2, k \pm 1/2)$ with a scale of 0.25. Seismograms are extracted using a similar strategy by summing the weighted records at a main node and sub-nodes of receiver locations.

A simulation example for a homogeneous model is presented in [Figure 3](#). P-wave velocity is 3 km/s, Q is 50, and a 200-m-thick vacuum layer is set at the top to simulate surface reflections. Acoustic and two kinds of viscoacoustic solvers are used to compute seismic wavefields, and the result of generalized standard linear solid (GSLs) method is used as a reference for comparison. Because of the phase dispersion and energy dissipation, viscoacoustic waves propagate faster than acoustic waves and have much weaker amplitudes ([Figures 3C,D](#)). The surface at the $z = 0$ km produces a reflection with opposite polarity compared with the direct wave ([Figure 3B](#)). The waveforms computed using the proposed method have good agreements with those of



GSLS in terms of both phases and amplitudes (red dot and black solid lines [Figures 3C,D](#)).

Numerical experiments

To test the performance of the proposed viscoacoustic modeling method, we apply it to a simple layer model and 2D/3D realistic Loess Plateau models. In the computation, the spatial accuracy of finite-difference is eighth order and the temporal accuracy is second order.

A simple layer model

The first example is a three layer model, of which the velocity and Q values are shown in [Figure 4A](#). A sinusoidal topography is designed to simulate the irregular surface. This model is discretized on a 601×501 grid with a 10-m spatial increment. A Ricker wavelet with the peak frequency of 15 Hz is used as the source time function. The source is deployed 10 m below the topography, and 501 receivers are evenly distributed horizontally on the observation surface. Time increment is 1 ms and duration is 6 s. [Figure 4B](#) shows the vertically distorted model in the computational domain. The topography has been fattened, but the originally horizontal interfaces in subsurface are curved. This coordinate conversion make it easy to simulate wave propagation in the near surface region.

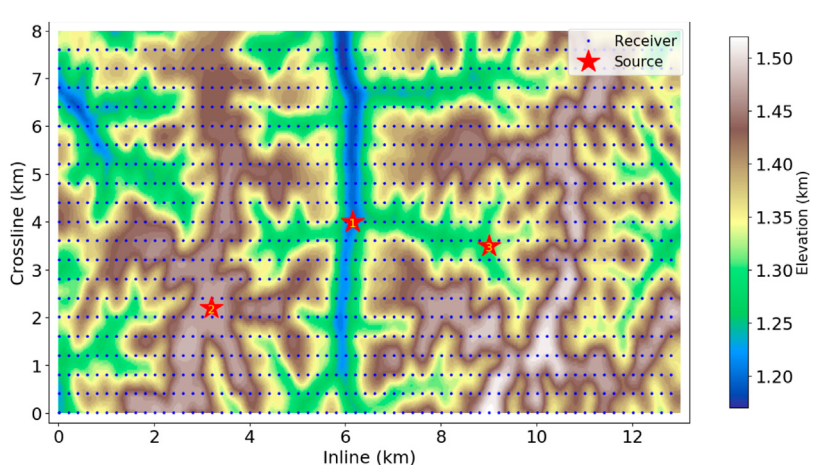
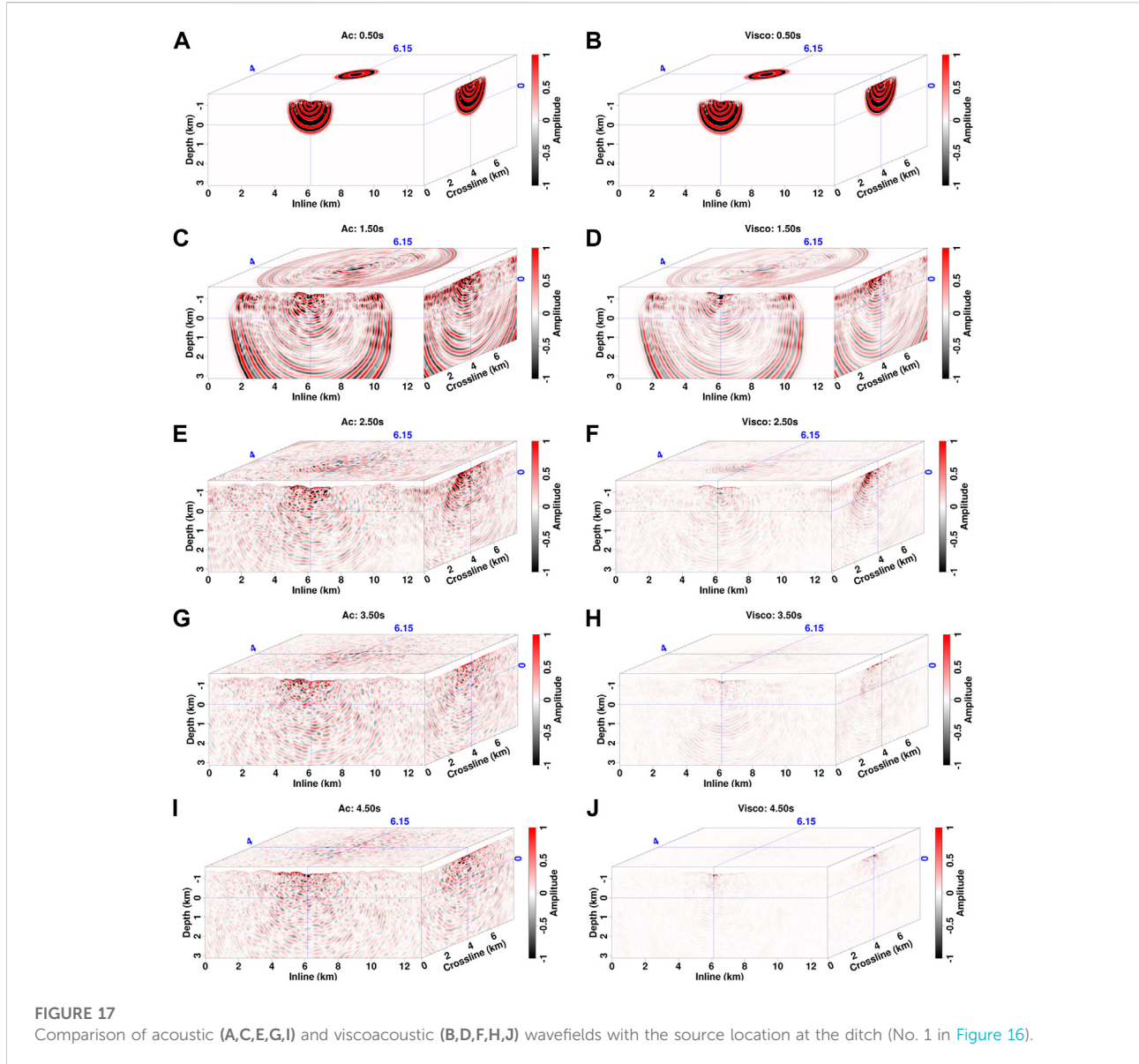


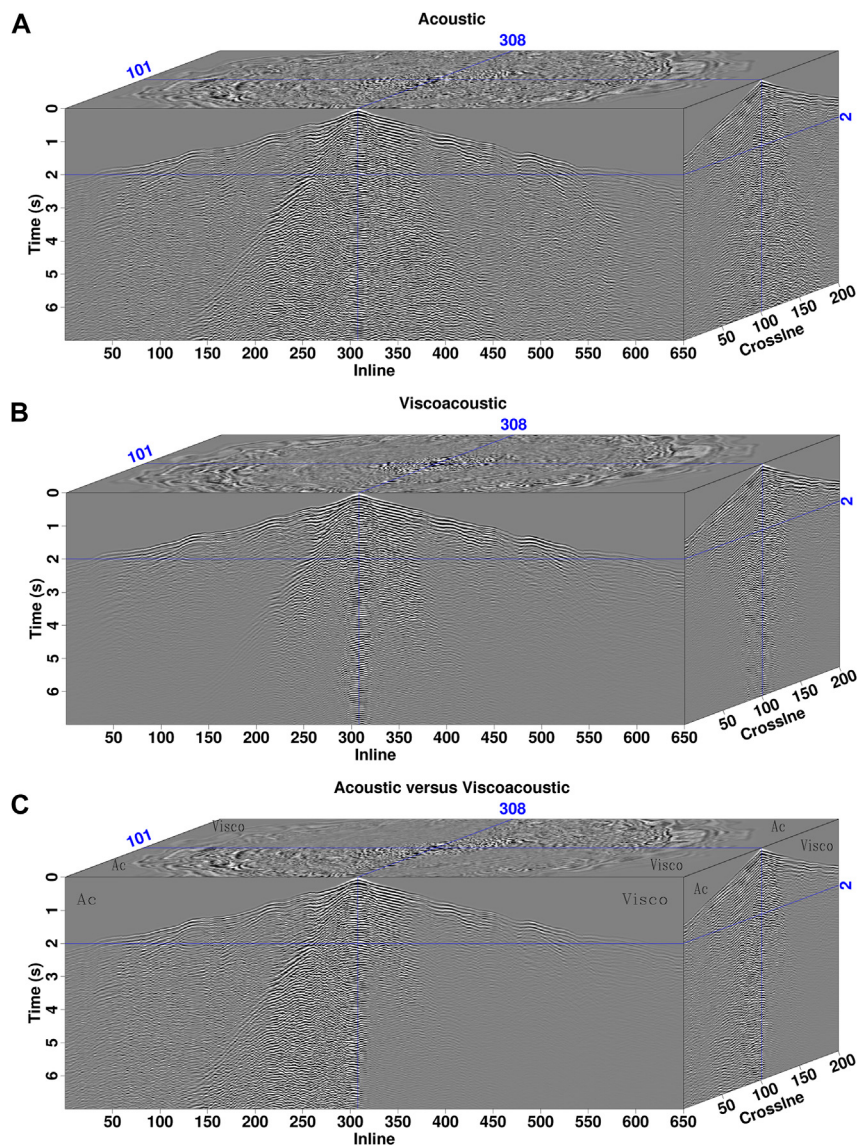
FIGURE 16
Source and receiver distributions of three observation systems for 3D wavefield models. Red stars denote the source locations of three experiments at the ditch (1), hill (2) and valley (3), and blue dots denote receivers.

**FIGURE 17**

Comparison of acoustic (**A,C,E,G,I**) and viscoacoustic (**B,D,F,H,J**) wavefields with the source location at the ditch (No. 1 in [Figure 16](#)).

The snapshots computed by solving the viscoacoustic and acoustic wave equations with and without the free surface are presented in [Figures 5, 6](#). In the computational domain, the wavefronts of direct and reflected waves are distorted because of c_x , c_y , and c_z coefficients in [Eq. 11](#) associated with the topography ([Figure 5A–C](#), [Figure 6A–C](#)). In contrast, in the physical domain, the direct wave becomes regular with a half-circle wavefront, and transmitted and reflected waves are generated at the interfaces ([Figure 5D–F](#), [Figure 6D–F](#)). The free surface at topography produces complicated boundary reflections, which intersects with deep effective wavefields ([Figures 6D–F](#)). Compared with acoustic modeling results, viscoacoustic wavefields have similar amplitudes and phases during early time, but they show considerably traveltime and amplitude differences as the propagation time increases ([Figure 7](#)).

The common-shot gathers are presented in [Figures 8, 9](#). For comparison, we also compute the record using the GSLS method and utilize it as a reference, in which three relaxation mechanisms are used to approximate a frequency-independent Q . Without the free surface, common-shot records only have a direct wave and two subsurface reflections. The direct waves computed using acoustic and viscoacoustic simulations have similar waveforms due to short propagation time. By contrast, the deep reflectors of viscoacoustic records, especially for the one from second interface, have different phases and much weaker amplitudes than acoustic records ([Figure 8D](#)). The GSLS benchmark result has a good agreement with that of the proposed method, indicating that the new method can accurately simulate viscoacoustic propagation with irregular topography (black solid lines and red dot lines in [Figures 8D, 9D](#)). In

**FIGURE 18**

Common-shot gathers of 3D Loess Plateau model with the source location at the ditch. (A) Acoustic modeling result, (B) viscoacoustic modeling result, and (C) comparison of acoustic (Ac) versus viscoacoustic (Visco) modeling results.

addition, the reflected events are no longer hyperbolic due to topographic surface, and incorporating the free surface in the modeling introduces many surface-related multiples (Figure 9).

2D Loess Plateau model

According to the outcrop of Chinese Loess Plateau, we build a realistic model for seismic modeling (Figure 10). Four layers are designed to mimic real loess structures: 1) a weathering layer with dry loess, 2) a low-velocity layer with wet loess, 3) a transition

layer with water saturated loess, and 4) a Tertiary soil layer. Detailed P-wave velocity and Q values of these layers are given in Table 2. The maximum thickness of loess is about 300 m (Figure 10A), and low Q values in the dry and wet loess layers can produce strong seismic attenuation. This model is discretized onto a $1,000 \times 2601$ grid with a 5-m spacing. The source is located at $x = 6.15$ km horizontally and $z = -1.18$ km vertically with a 15-Hz Ricker wavelet as the source time function. The projected velocity in the computational domain is shown in Figure 10B, of which the surface is flattened and subsurface structures are slightly distorted.

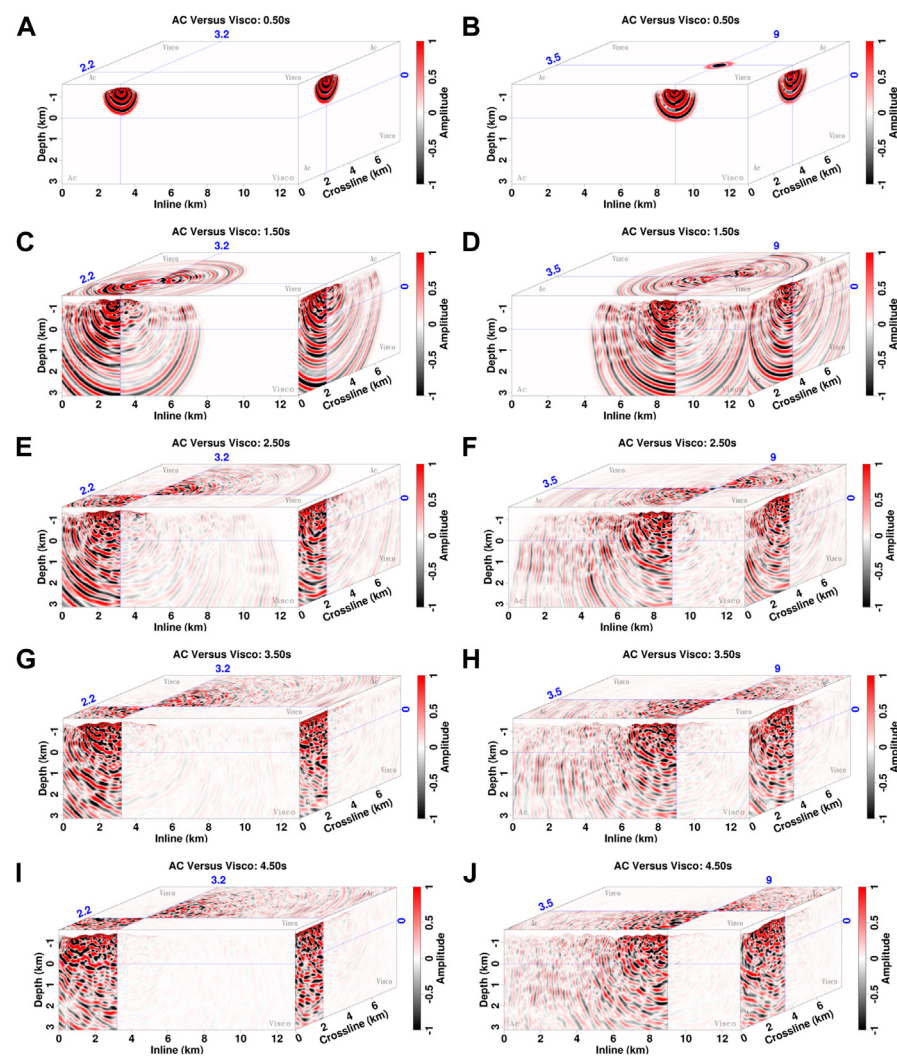


FIGURE 19

Comparison of acoustic and viscoacoustic wavefields with the source locations at the hill [(A,C,E,G,I), No. 2 in Figure 16] and valley [(B,D,F,H,J), No. 3 in Figure 16].

The snapshots in the computational domain and physical space computed with and without the free surface are shown in Figures 11, 12. With a top absorption boundary condition, the reflected waves of subsurface interfaces can be clearly distinguished from direct waves (Figure 11). The wavefronts in the computational domain are slightly distorted and appear to be non-continuous because of irregular topography (left column in Figure 11). After mapping back to the physical domain, the wavefields, especially for reflections, have regular half-circle wavefronts (right column in Figure 11). By setting the topography as a free surface, seismic waves propagate back and forth between top surface and loess bottom vertically and between hill and ditch horizontally, resulting in strong multiple-like scatterings. These scatterings contaminate

effective reflections generated from deep interfaces (Figure 12). Comparisons between acoustic and viscoacoustic modeling show a similar result as in the example of layer model (Figure 13). Their waveforms are similar when the propagation time is less than 0.5 s (Figure 13A). But as the time increases to 1 s, the difference of phases and amplitudes can be visually observed (Figure 13B). With a further longer duration, viscoacoustic wavefields have considerably weaker amplitudes than acoustic modeling results (Figures 13C,D).

The corresponding common-shot gathers are presented in Figure 14. Large velocity contrasts between loess layers and basement produce complicated refractions around the first break, and irregular topography results in distorted non-hyperbolic

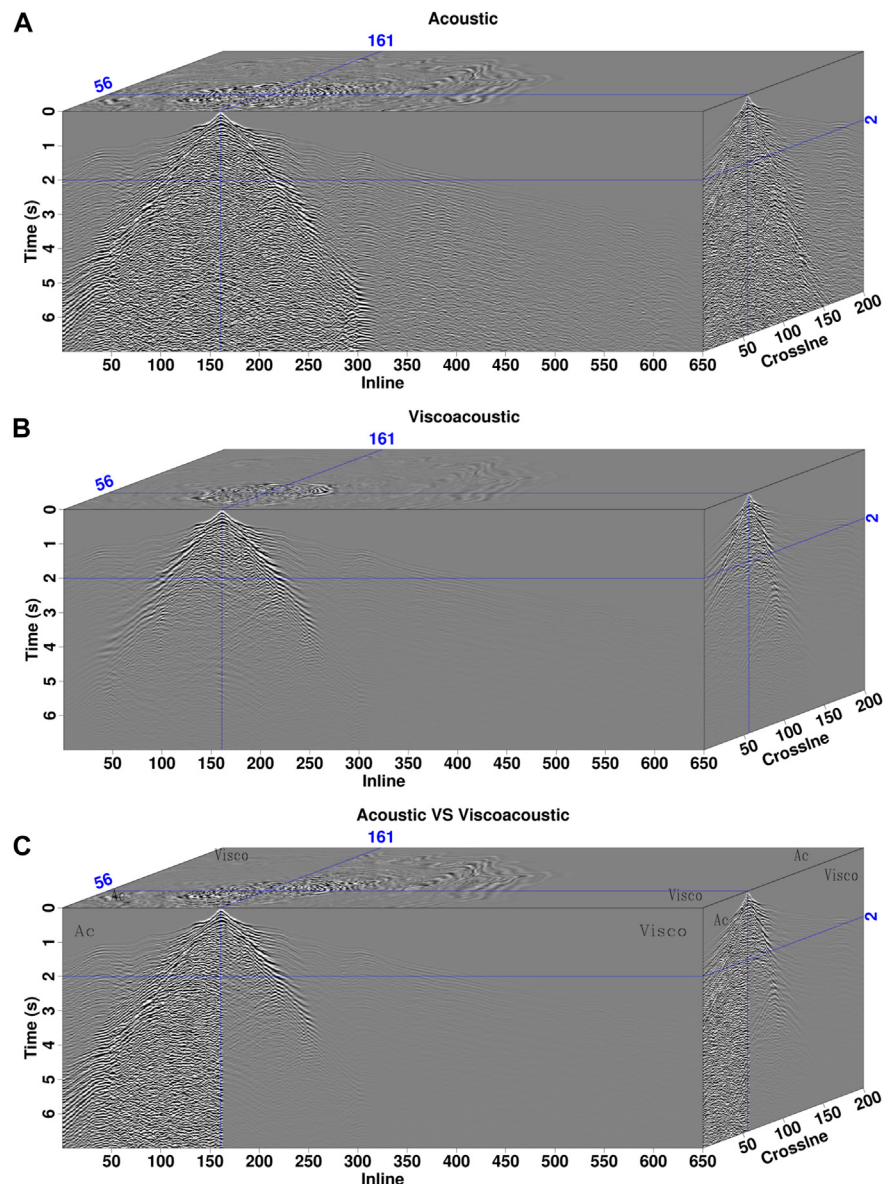


FIGURE 20
(A–C) Common-shot gathers of 3D Loess Plateau model with the source location at the hill. The panel notations are the same as those in Figure 18.

reflections (Figure 14A). Incorporating the free surface into viscoacoustic modeling produces strong scattering noises near the direct wave, and deep effective reflections are totally submerged in the noise (Figure 14B). For comparison, we also compute acoustic records using the same model and observation settings. Similar to the analysis for snapshots, the events at a short time have similar phases and amplitudes on acoustic and viscoacoustic records (Figures 14C,D). But considerable difference of deep reflections can be observed as the time increases due to attenuation-related phase dispersion and amplitude dissipation. In addition, large-offset

refractions and scatterings near direct wave of viscoacoustic record are much weaker than those of acoustic modeling results. This is caused by strong attenuation in the low-Q loess layers.

3D Loess Plateau model

Because 2D modeling cannot accurately simulate the amplitudes of seismic waves, we apply the proposed viscoacoustic modeling method to a more realistic 3D model (Figure 15). Compared with 2D

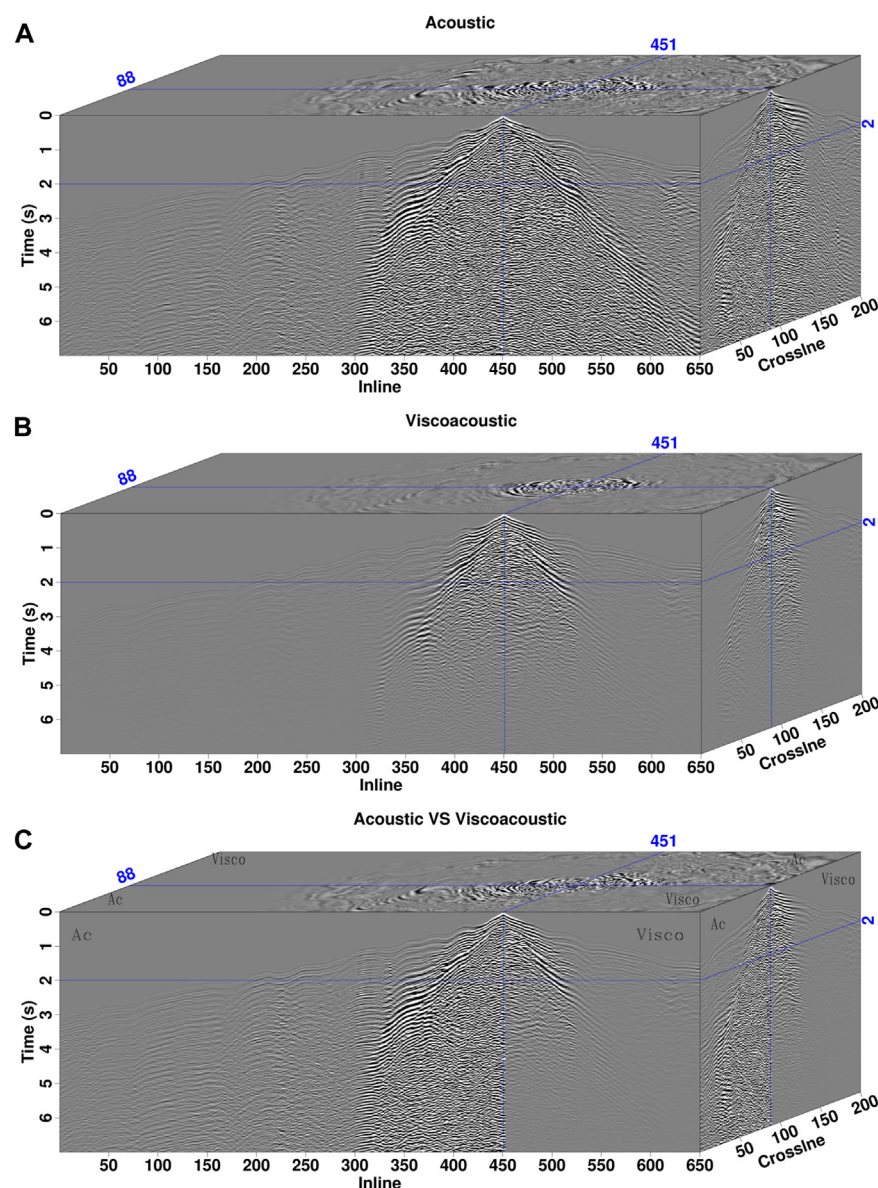
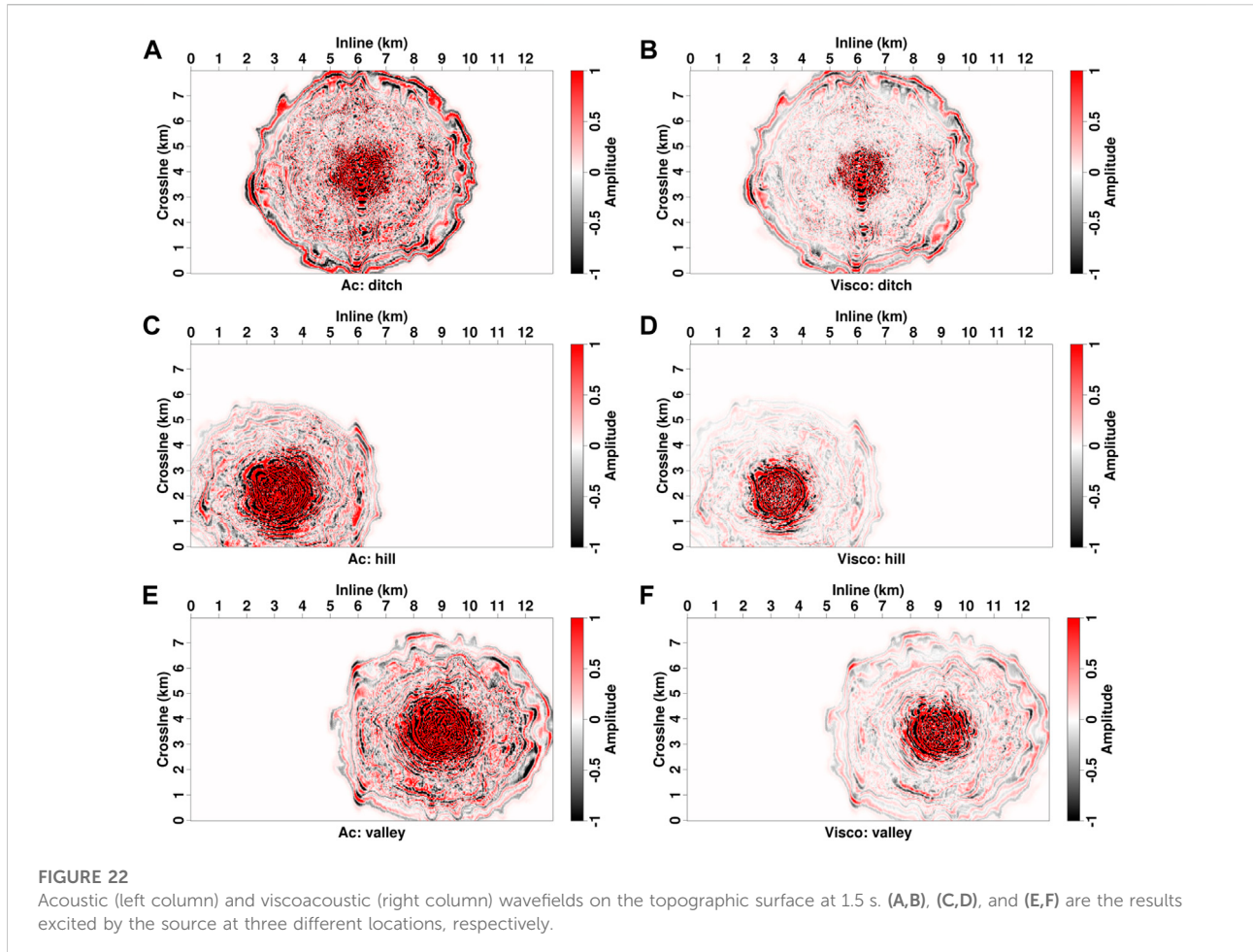


FIGURE 21
(A–C) Common-shot gathers of 3D Loess Plateau model with the source location at the valley. The panel notations are the same as those in Figure 18.

Loess Plateau model, geographic characteristics of loess distribution, including typical ditch, hill and valley, are more clearly visible in the 3D model. The setting for Q in shallow loess layers is the same to that in 2D model. For deep sandstone strata, the well-logging data and rock physics analysis show that P-wave velocity and Q models crudely satisfy an empirical relation as $Q = \sqrt{v_p}$, where v_p denotes P-wave velocity with the unit of m/s. This model is discretized by $475 \times 1,301 \times 800$ nodes with a 10-m increment. 650×200 receivers along inline and crossline directions are uniformly deployed to record seismograms (blue dots in Figure 16). Three experiments are

carried out with sources in the ditch, hill and valley, respectively (red stars in Figure 16). Time increment in the finite-difference is 0.5 ms and duration is 7 s.

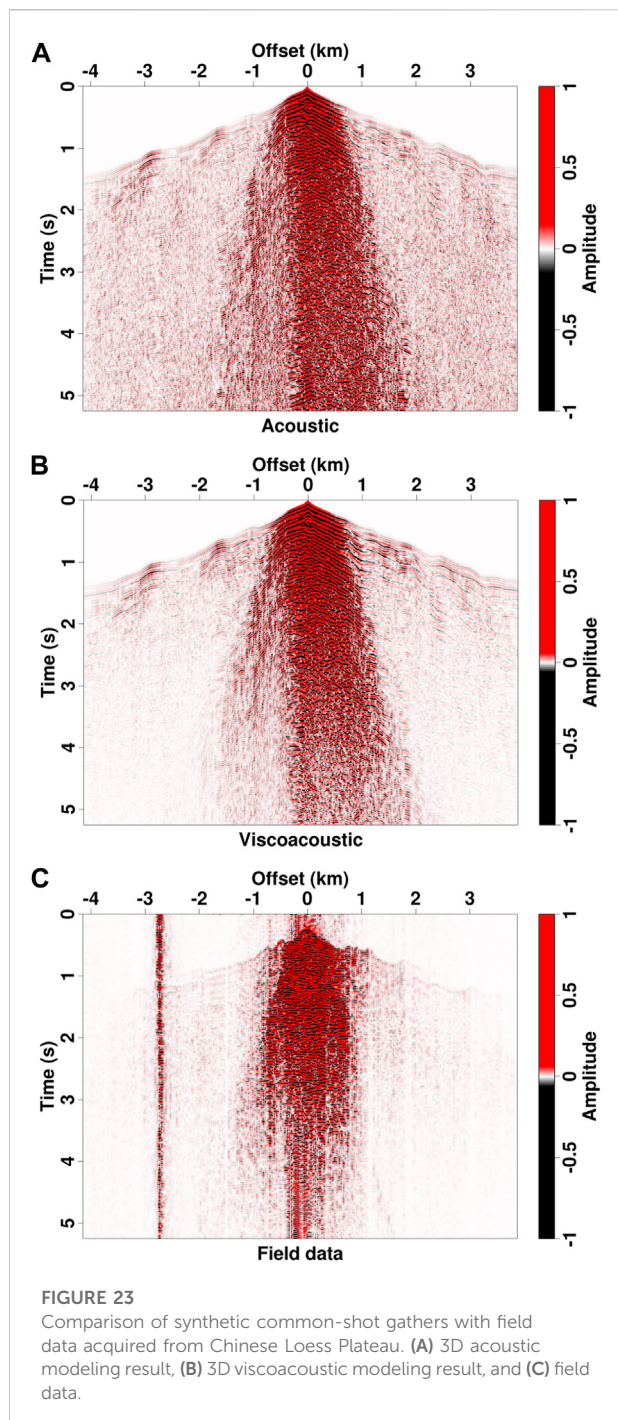
The snapshots and common-shot gathers are presented in Figures 17, 18. Similar to 2D modeling, the interactions between topographic free-surface and loess bottom produces strong scatterings in near-surface region, which contaminate deep reflections (Figure 17). This leads to typical “black-triangle” noise below the source location in the records (Figure 18A). Without subsequent processing, it is difficult to visually find hyperbolic reflections. Because of the geometric



spreading in a 3D volume, wavefield amplitude decays faster during propagation than in the 2D case. In addition, seismic attenuation introduces strong amplitude dissipation for viscoacoustic waves (right column in Figure 17). This results in rather weak amplitudes at large-offset traces and large observation time compared with acoustic recordings (Figures 18B,C).

The modeling results of the other two experiments are shown in Figures 19–21. Thicker loess sediments in the hill and valley produce stronger attenuation effect on seismic waves than that in the ditch, resulting in large amplitude and phase difference between acoustic and viscoacoustic snapshots (Figure 19). The phase dispersion and amplitude dissipation of viscoacoustic recordings become more pronounced. The waveforms with large offsets and times, including near-surface-related scatterings and deep reflections, are attenuated quickly (Figures 20, 21). In contrast to acoustic recordings, no events can be observed visually at the time greater than 5 s. The low SNR and weak amplitudes of recordings pose a great challenge for subsequent seismic data processing and imaging.

Figure 22 shows the snapshots of 1.5 s on the observation surface for three experiments. In the first experiment, strong scatterings are generated and propagate along the north-south ditch (Figures 22A,B). This is because the loess in the ditch was eroded, and the outcrop has a relative higher velocity than the loess. In contrast, the experiments excited on the hill and valley show an isotropic scattering pattern (Figures 22C–F). In addition, the wavefields excited by the source on the hill are affected by attenuation more largely than those excited in the ditch and valley (Figures 22D,F). Comparisons of acoustic modeling result, viscoacoustic modeling result and a common-shot gather acquired from Chinese Loess Plateau are presented in Figure 23. Note that both acoustic and viscoacoustic modeling can simulate strong black-triangle scattering noise below the direct waves, which has a consistent kinematic pattern with the field data. But acoustic records have relatively stronger amplitudes for the time greater than 3 s (Figure 23B). By incorporating seismic attenuation, viscoacoustic modeling produces weak amplitudes for large-duration and large-offset events, which have a good agreement with the amplitude characteristic of field data (Figure 23C).



Discussion

To study wave propagations in the Loess Plateau, we propose a viscoacoustic modeling method based upon a wave equation with the explicitly expressed Q . It does not need to convert Q to strain and stress relaxation times as in the GSLS method. But compared with the fractional Laplacian complex-valued wave equations (Zhu and Harris,

2014; Yang and Zhu, 2018), the proposed equation does not separate the dispersion and dissipation terms. This makes it not as easy as Zhu and Harris (2014) and Yang and Zhu (2018)'s methods to directly compensate for Q effect in the reverse-time migration. An appropriate Q -compensation strategy will be investigated for seismic imaging in the future.

In this study, we do not incorporate the elasticity and anisotropy into wavefield modeling, and therefore cannot simulate S-wave propagation and P-S conversion. More accurate wavefield simulation should be extended to an anisotropic and anelastic medium, which can describe both P- and S-wave propagations in the Loess Plateau. But for elastic modeling, the S-wave velocity of loess layers can be as low as 200–300 m/s. This requires a very fine grid (< 5 m) to avoid numerical dispersion in the finite-difference modeling method, which will significantly increase the computational cost. A combined grid strategy, which uses a curvilinear grid in the near-surface zone and a regular Cartesian grid at depth, can be introduced to alleviate the computational burden (Sjögren and Petersson, 2012). In addition, the spectral-element method based on a spatially varying grid is another way to accurately simulate anisotropic and (an)elastic wave propagation in the Loess Plateau (Komatsch and Tromp, 1999).

From 2D/3D modeling results for the Loess Plateau model, there is strong black-triangle scattering noise below the direct waves, which is consistent with the field observation. The generation mechanism of this type noise is similar to that of interval multiples, which results from the wave propagation back and forth between top free surface and loess bottom vertically and between hill and ditch horizontally. If incorporating elasticity in the modeling, surface waves will interact with the scatterings and produce more complicated noise. In subsequent processing, it is critical to remove the effect of strong black-triangle noise to produce a high-quality image, and therefore advanced signal processing techniques should be adopted to suppress loess-related noise.

Conclusion

We present a 2D/3D viscoacoustic modeling method in this work and apply it to simulate wave propagation in the Loess Plateau. A viscoacoustic wave equation with the explicitly expressed Q is first derived to describe the phase dispersion and amplitude dissipation. Then, a vertically deformed grid is used to conform to the topographic surface, which build a mapping relation between physical space and computational domain. To accurately compute the spatial derivatives, a fully staggered-grid finite-difference scheme is utilized to solve the viscoacoustic wave equation in the deformed grid. Numerical experiments demonstrate that the proposed method can accurately simulate viscoacoustic

wave propagation in the Loess Plateau models. The 3D modeling results show consistent kinematic and dynamic characteristics with the field data acquired from the Loess Plateau in China.

Data availability statement

The original contributions presented in the study are included in the article/supplementary material, further inquiries can be directed to the corresponding author.

Author contributions

ZH presented the idea, JY, LH, JH, and SQ developed the code, did the tests and wrote the manuscript. JS and YY revised the manuscript.

Funding

This study is funded by the CNPC project of viscoacoustic wave equation modeling and reverse-time migration (no. HX20220326), and the startup funding (no. 20CX06069A) of Guanghua Scholar at China University of Petroleum (East China). The work was carried out at National Supercomputer Center in Tianjin, and this research was supported by Tianhe Qingsuo Project-special fund project in the field of geoscience.

References

- Aki, K., and Richards, P. G. (2002). *Quantitative seismology*. United States: University Science Books.
- Beydoun, W. B., and Keho, T. H. (1987). The paraxial ray method. *Geophysics* 52, 1639–1653. doi:10.1190/1.1442281
- Bording, R. P., and Lines, L. R. (1997). *Seismic modeling and imaging with the complete wave equation*. Houston, Texas, United States: Society of Exploration Geophysicists.
- Carcione, J. M., Herman, G. C., and ten Kroode, A. P. E. (2002). Seismic modeling. *Geophysics* 67, 1304–1325. doi:10.1190/1.1500393
- Carcione, J. M., Poletto, F., and Gei, D. (2004). 3-D wave simulation in anelastic media using the Kelvin–Voigt constitutive equation. *J. Comput. Phys.* 196, 282–297. doi:10.1016/j.jcp.2003.10.024
- Carcione, J. M. (1993). Seismic modeling in viscoelastic media. *Geophysics* 58, 110–120. doi:10.1190/1.1443340
- Carcione, J. M. (2007). *Wave fields in real media: Wave propagation in anisotropic, anelastic, porous and electromagnetic media*. Amsterdam, Netherlands: Elsevier.
- Carcione, J. M. (1990). Wave propagation in anisotropic linear viscoelastic media: Theory and simulated wavefields. *Geophys. J. Int.* 101, 739–750. doi:10.1111/j.1365-246X.1990.tb05580.x
- Červený, V., Klimeš, L., and Pšenčík, I. (2007). “Seismic ray method: Recent developments,” in *Advances in wave propagation in heterogeneous Earth*. Editors R.-S. Wu, V. Maupin, and R. Dmowska (Amsterdam, Netherlands: Elsevier), 1–126. doi:10.1016/S0065-2687(06)48001-8
- Červený, V., Popov, M. M., and Pšenčík, I. (1982). Computation of wave fields in inhomogeneous media-Gaussian beam approach. *Geophys. J. Int.* 70, 109–128. doi:10.1111/j.1365-246x.1982.tb06394.x
- Červený, V. (2001). *Seismic ray theory*. Cambridge, United Kingdom: Cambridge University Press.
- Chapman, H., and Drummond, R. (1982). Body-wave seismograms in inhomogeneous media using Maslov asymptotic theory. *Bull. Seismol. Soc. Am.* 72, S277–S317. doi:10.1785/BSSA07206B0277
- Chen, H., Zhou, H., Li, Q., and Wang, Y. (2016). Two efficient modeling schemes for fractional Laplacian viscoacoustic wave equation. *GEOPHYSICS* 81, T233–T249. doi:10.1190/geo2015-0660.1
- De Basabe, J. D., and Sen, M. K. (2009). New developments in the finite-element method for seismic modeling. *Lead. Edge* 28, 562–567. doi:10.1190/1.3124931
- de la Puente, J., Ferrer, M., Hanzich, M., Castillo, J. E., and Cela, J. M. (2014). Mimetic seismic wave modeling including topography on deformed staggered grids. *Geophysics* 79, T125–T141. doi:10.1190/geo2013-0371.1
- Emmerich, H., and Korn, M. (1987). Incorporation of attenuation into time-domain computations of seismic wave fields. *GEOPHYSICS* 52, 1252–1264. doi:10.1190/1.1442386
- Etgen, J. T., and O’Brien, M. J. (2007). Computational methods for large-scale 3D acoustic finite-difference modeling: A tutorial. *Geophysics* 72, SM223–SM230. doi:10.1190/1.2753753
- Fichtner, A., and van Driel, M. (2014). Models and Fréchet kernels for frequency-(in)dependent q. *Geophys. J. Int.* 198, 1878–1889. doi:10.1093/gji/ggu228
- Gray, S. H., and May, W. P. (1994). Kirchhoff migration using eikonal equation traveltimes. *Geophysics* 59, 810–817. doi:10.1190/1.1443639

Acknowledgments

We are thankful for the support from the Funds of the National Key R&D Program of China (no. 2019YFC0605503), the Major Scientific and Technological Projects of CNPC (no. ZD 2019-183-003), the Major projects during the 14th Five-year Plan period (no. 2021QNLM020001), the National Outstanding Youth Science Foundation (no. 41922028), and Creative Research Groups of China (no. 41821002).

Conflict of interest

The authors ZH and LH were employed by Research Institute of Petroleum Exploration and Development-Northwest PetroChina.

The remaining authors declare that the research was conducted in the absence of any commercial or financial relationships that could be construed as a potential conflict of interest.

Publisher's note

All claims expressed in this article are solely those of the authors and do not necessarily represent those of their affiliated organizations, or those of the publisher, the editors and the reviewers. Any product that may be evaluated in this article, or claim that may be made by its manufacturer, is not guaranteed or endorsed by the publisher.

- Guo, P., and McMechan, G. A. (2017). Evaluation of three first-order isotropic viscoelastic formulations based on the generalized standard linear solid. *J. Seismic Explor.* 26, 199–226.
- Guo, P., McMechan, G. A., and Ren, L. (2019). Modeling the viscoelastic effects in p-waves with modified viscoacoustic wave propagation. *Geophysics* 84, T381–T394. doi:10.1190/geo2018-0747.1
- Hestholm, S., and Ruud, B. (1994). 2D finite-difference elastic wave modelling including surface topography1. *Geophys. Prospect.* 42, 371–390. doi:10.1111/j.1365-2478.1994.tb00216.x
- Hestholm, S., and Ruud, B. (1998). 3-D finite-difference elastic wave modeling including surface topography. *Geophysics* 63, 613–622. doi:10.1190/1.1444360
- Hestholm, S., and Ruud, B. (2002). 3d free-boundary conditions for coordinate-transform finite-difference seismic modelling. *Geophys. Prospect.* 50, 463–474. doi:10.1046/j.1365-2478.2002.00327.x
- Hestholm, S. (1999). Three-dimensional finite difference viscoelastic wave modelling including surface topography. *Geophys. J. Int.* 139, 852–878. doi:10.1046/j.1365-246x.1999.00994.x
- Hill, R. (1990). Gaussian beam migration. *Geophysics* 55, 1416–1428. doi:10.1190/1.1442788
- Hill, R. (2001). Prestack Gaussian-beam depth migration. *Geophysics* 66, 1240–1250. doi:10.1190/1.1487071
- Jastram, C., and Tessmer, E. (1994). Elastic modelling on a grid with vertically varying spacing1. *Geophys. Prospect.* 42, 357–370. doi:10.1111/j.1365-2478.1994.tb00215.x
- Julian, B., and Gubbins, D. (1977). Three-dimensional seismic ray tracing. *J. Geophys.* 43, 95–113.
- Kendall, J., and Thomson, C. (1993). Maslov ray summation, pseudo-caustics, Lagrangian equivalence and transient seismic waveforms. *Geophys. J. Int.* 113, 186–214. doi:10.1111/j.1365-246x.1993.tb02539.x
- Kjartansson, E. (1979). Constant Q-wave propagation and attenuation. *J. Geophys. Res.* 84, 4737–4748. doi:10.1029/JB084iB09p04737
- Koene, E. F. M., Robertsson, J. O. A., and Andersson, F. (2021). Anisotropic elastic finite-difference modeling of sources and receivers on Lebedev grids. *Geophysics* 86, A21–A25. doi:10.1190/geo2020-0522.1
- Komatitsch, D., Barnes, C., and Tromp, J. (2000). Simulation of anisotropic wave propagation based upon a spectral element method. *Geophysics* 65, 1251–1260. doi:10.1190/1.1444816
- Komatitsch, D., Erlebacher, G., Göddeke, D., and Michéa, D. (2010). High-order finite-element seismic wave propagation modeling with mpi on a large gpu cluster. *J. Comput. Phys.* 229, 7692–7714. doi:10.1016/j.jcp.2010.06.024
- Komatitsch, D., Ritsema, J., and Tromp, J. (2002). The spectral-element method, beowulf computing, and global seismology. *Science* 298, 1737–1742. doi:10.1126/science.1076024
- Komatitsch, D., and Tromp, J. (1999). Introduction to the spectral element method for three-dimensional seismic wave propagation. *Geophys. J. Int.* 139, 806–822. doi:10.1046/j.1365-246x.1999.00967.x
- Komatitsch, D., and Tromp, J. (2002). Spectral-element simulations of global seismic wave propagation—I. Validation. *Geophys. J. Int.* 149, 390–412. doi:10.1046/j.1365-246X.2002.01653.x
- Konuk, T., and Shragge, J. (2020). Modeling full-wavefield time-varying sea-surface effects on seismic data: A mimetic finite-difference approach. *Geophysics* 85, T45–T55. doi:10.1190/geo2019-0181.1
- Kristek, J., and Moczo, P. (2003). Seismic-wave propagation in viscoelastic media with material discontinuities: A 3D fourth-order staggered-grid finite-difference modeling. *Bull. Seismol. Soc. Am.* 93, 2273–2280. doi:10.1785/0120030023
- Lebedev, V. (1964). Difference analogues of orthogonal decompositions, basic differential operators and some boundary problems of mathematical physics. i. *USSR Comput. Math. Math. Phys.* 4, 69–92. doi:10.1016/0041-5553(64)90240-X
- Lei, W., Ruan, Y., Bozda, E., Peter, D., Lefebvre, M., Komatitsch, D., et al. (2020). Global adjoint tomography—Model GLAD-M25. *Geophys. J. Int.* 223, 1–21. doi:10.1093/gji/ggaa253
- Levander, A. R. (1988). Fourth-order finite-difference p-sv seismograms. *Geophysics* 53, 1425–1436. doi:10.1190/1.1442422
- Liao, Q., and McMechan, G. A. (1996). Multifrequency viscoacoustic modeling and inversion. *Geophysics* 61, 1371–1378. doi:10.1190/1.1444060
- Lisitsa, V., and Vishnevskiy, D. (2010). Lebedev scheme for the numerical simulation of wave propagation in 3d anisotropic elasticity. *Geophys. Prospect.* 58, 619–635. doi:10.1111/j.1365-2478.2009.00862.x
- Liu, H.-P., Anderson, D. L., and Kanamori, H. (1976). Velocity dispersion due to anelasticity: Implications for seismology and mantle composition. *Geophys. J. Int.* 47, 41–58. doi:10.1111/j.1365-246X.1976.tb01261.x
- Marfurt, K. J. (1984). Accuracy of finite-difference and finite-element modeling of the scalar and elastic wave equations. *Geophysics* 49, 533–549. doi:10.1190/1.1441689
- Maslov, V., Arnold, V., and Buslaev, V. S. (1972). *Theory of perturbations and asymptotic methods*. Russia: Moscow University Press.
- McMechan, G. A. (1989). A review of seismic acoustic imaging by reverse-time migration. *Int. J. Imaging Syst. Technol.* 1, 18–21. doi:10.1002/ima.1850010104
- Mittet, R. (2002). Free-surface boundary conditions for elastic staggered-grid modeling schemes. *Geophysics* 67, 1616–1623. doi:10.1190/1.1512752
- Mulder, W., and Plessix, R. (2008). Exploring some issues in acoustic full waveform inversion. *Geophys. Prospect.* 56, 827–841. doi:10.1111/j.1365-2478.2008.00708.x
- Müller, G. (1984). Efficient calculation of Gaussian-beam seismograms for two-dimensional inhomogeneous media. *Geophys. J. Int.* 79, 153–166. doi:10.1111/j.1365-246x.1984.tb02847.x
- Nakamura, T., Takenaka, H., Okamoto, T., and Kaneda, Y. (2012). Fdm simulation of seismic-wave propagation for an aftershock of the 2009 suruga bay earthquake: Effects of ocean-bottom topography and seawater layer. *Bull. Seismol. Soc. Am.* 102, 2420–2435. doi:10.1785/0120110356
- Nowack, R., and Aki, K. (1984). The two-dimensional Gaussian beam synthetic method: Testing and application. *J. Geophys. Res.* 89, 7797–7819. doi:10.1029/jb089ib09p07797
- Robertsson, J. O. (1996). A numerical free-surface condition for elastic/viscoelastic finite-difference modeling in the presence of topography. *Geophysics* 61, 1921–1934. doi:10.1190/1.1444107
- Shragge, J., and Tapley, B. (2017). Solving the tensorial 3d acoustic wave equation: A mimetic finite-difference time-domain approach. *Geophysics* 82, T183–T196. doi:10.1190/geo2016-0691.1
- Sjögren, B., and Petersson, N. A. (2012). A fourth order accurate finite difference scheme for the elastic wave equation in second order formulation. *J. Sci. Comput.* 52, 17–48. doi:10.1007/s10915-011-9531-1
- Stekl, I., and Pratt, R. G. (1998). Accurate viscoelastic modeling by frequency-domain finite differences using rotated operators. *Geophysics* 63, 1779–1794. doi:10.1190/1.1444472
- Sun, J. (2002). Provenance of loess material and formation of loess deposits on the Chinese loess plateau. *Earth Planet. Sci. Lett.* 203, 845–859. doi:10.1016/S0012-821X(02)00921-4
- Sun, J., Zhu, T., and Fomel, S. (2015). Viscoacoustic modeling and imaging using low-rank approximation. *Geophysics* 80, A103–A108. doi:10.1190/geo2015-0083.1
- Sun, Y., Zhang, W., and Chen, X. (2016). Seismic-wave modeling in the presence of surface topography in 2D general anisotropic media by a curvilinear grid finite-difference method. *Bull. Seismol. Soc. Am.* 106, 1036–1054. doi:10.1785/0120150285
- Sun, Y., Zhang, W., Ren, H., Bao, X., Xu, J., Sun, N., et al. (2021). 3D seismic-wave modeling with a topographic fluid-solid interface at the sea bottom by the curvilinear-grid finite-difference method. *Bull. Seismol. Soc. Am.* 111, 2753–2779. doi:10.1785/0120200363
- Tape, C., Liu, Q., Maggi, A., and Tromp, J. (2009). Adjoint tomography of the southern California crust. *Science* 325, 988–992. doi:10.1126/science.1175298
- Um, J., and Thurber, C. (1987). A fast algorithm for two-point seismic ray tracing. *Bull. Seismol. Soc. Am.* 77, 972–986. doi:10.1785/BSSA0770030972
- Vigh, D., Starr, E. W., and Kapoor, J. (2009). Developing Earth models with full waveform inversion. *Lead. Edge* 28, 432–435. doi:10.1190/1.3112760
- Virieux, J., and Operto, S. (2009). An overview of full-waveform inversion in exploration geophysics. *Geophysics* 74, WCC1–WCC26. doi:10.1190/1.3238367
- Virieux, J., Operto, S., Ben-Hadj-Ali, H., Brossier, R., Etienne, V., Sourbier, F., et al. (2009). Seismic wave modeling for seismic imaging. *Lead. Edge* 28, 538–544. doi:10.1190/1.3124928
- Virieux, J. (1986). P-SV wave propagation in heterogeneous media: Velocity-stress finite-difference method. *Geophysics* 51, 889–901. doi:10.1190/1.1442147

- Wang, D., Gao, J., Li, Y., Xia, Z., and Wang, B. (2004). Mesozoic reservoir prediction in the longdong loess plateau. *Appl. Geophys.* 1, 20–25. doi:10.1007/s11770-004-0023-z
- Wang, N., Xing, G., Zhu, T., Zhou, H., and Shi, Y. (2022). Propagating seismic waves in vti attenuating media using fractional viscoelastic wave equation. *JGR. Solid Earth* 127, e2021JB023280. doi:10.1029/2021jb023280
- Wang, X., Zhang, L., Liang, Q., Jiang, C., Wang, W., Xiaolong, Y., et al. (2014). *Full-azimuth, high-density, 3d point-source/point-receiver seismic survey for shale gas exploration in a Loess Plateau: A case study from the ordos basin, China*. United States: First Break, 32.
- Wang, Z., Li, J., Wang, B., Xu, Y., and Chen, X. (2017). Time-domain explicit finite-difference method based on the mixed-domain function approximation for acoustic wave equation. *Geophysics* 82, T237–T248. doi:10.1190/geo2017-0012.1
- Wu, W., Lines, L. R., and Lu, H. (1996). Analysis of higher-order, finite-difference schemes in 3-D reverse-time migration. *Geophysics* 61, 845–856. doi:10.1190/1.1444009
- Xing, G., and Zhu, T. (2019). Modeling frequency-independent q viscoacoustic wave propagation in heterogeneous media. *J. Geophys. Res. Solid Earth* 124, 11568–11584. doi:10.1029/2019jb017985
- Yang, D., Liu, E., Zhang, Z., and Teng, J. (2002). Finite-difference modelling in two-dimensional anisotropic media using a flux-corrected transport technique. *Geophys. J. Int.* 148, 320–328. doi:10.1046/j.1365-246x.2002.01012.x
- Yang, J., Huang, J., Zhu, H., McMechan, G., and Li, Z. (2022). Introduction to a two-way beam wave method and its applications in seismic imaging. *JGR. Solid Earth* 127, e2021JB023357. doi:10.1029/2021jb023357
- Yang, J., and Zhu, H. (2018). A time-domain complex-valued wave equation for modelling visco-acoustic wave propagation. *Geophys. J. Int.* 215, 1064–1079. doi:10.1093/gji/ggy323
- Yang, J., Zhu, H., Li, X., Ren, L., and Zhang, S. (2020). Estimating p wave velocity and attenuation structures using full waveform inversion based on a time domain complex-valued viscoacoustic wave equation: The method. *J. Geophys. Res. Solid Earth* 125, e2019JB019129. doi:10.1029/2019jb019129
- Yang, J., Zhu, H., McMechan, G., and Yue, Y. (2018). Time-domain least-squares migration using the Gaussian beam summation method. *Geophys. J. Int.* 214, 548–572. doi:10.1093/gji/ggy142
- Yao, J., Zhu, T., Hussain, F., and Kouri, D. J. (2017). Locally solving fractional laplacian viscoacoustic wave equation using hermite distributed approximating functional method. *Geophysics* 82, T59–T67. doi:10.1190/geo2016-0269.1
- Zhang, W., Zhang, Z., and Chen, X. (2012). Three-dimensional elastic wave numerical modelling in the presence of surface topography by a collocated-grid finite-difference method on curvilinear grids. *Geophys. J. Int.* 190, 358–378. doi:10.1111/j.1365-246X.2012.05472.x
- Zhu, T., and Harris, J. M. (2014). Modeling acoustic wave propagation in heterogeneous attenuating media using decoupled fractional laplacians. *Geophysics* 79, T105–T116. doi:10.1190/geo2013-0245.1

Appendix A: Stability condition for the finite-difference onto a vertical stretched grid

According the energy analysis method (Yang et al., 2002), the stability of the finite-difference solver for Eq. 13 requires the time and space increments satisfying

$$\Delta t^2 \left(1 + \frac{s}{Q} \right) \left[\left(\frac{1}{\Delta\alpha} + c_x \frac{1}{\Delta\gamma} \right)^2 + \left(\frac{1}{\Delta\beta} + c_y \frac{1}{\Delta\gamma} \right)^2 + \left(c_z \frac{1}{\Delta\gamma} \right)^2 \right] \leq \frac{1}{v^2} \quad (\text{A1})$$

If the spatial increments are the same, i.e., $\Delta h = \Delta\alpha = \Delta\beta = \Delta\gamma$, we have

$$\frac{\Delta t^2}{\Delta h^2} \left(1 + \frac{s}{Q} \right) \left[(1 + c_x)^2 + (1 + c_y)^2 + (c_z)^2 \right] \leq \frac{1}{v^2} \quad (\text{A2})$$

Incorporating the finite-difference coefficients, the time interval has to satisfy

$$\Delta t \leq \frac{\Delta h}{c v \sqrt{\left(1 + \frac{s}{Q} \right) \left[(1 + c_x)^2 + (1 + c_y)^2 + (c_z)^2 \right]}}, \quad (\text{A3})$$

where c is the summation of finite-difference coefficients. Considering the varying velocity, Q and topography slope, Eq. A3 reduces to Eq. 14.